Development and Validation of a High-Fidelity Aero-Thermo-Elastic Analysis Capability

Soudeh Kamali[1], Dimitri J. Mavriplis[2], and Evan M. Anderson[3]
Department of Mechanical Engineering, University of Wyoming, Laramie, WY, 82070, USA

Coupled aero-thermal-elastic simulations are required for the accurate simulation of many high speed flow problems. Hence, the multidisciplinary analysis of such problems is the main focus of the current work. In this study, the flow simulations are carried out using NSU3D, a three-dimensional implicit finite volume solver developed in-house that has been well tested and validated through numerous previous studies. For the thermal and structural solutions, a finite-element solver called AStrO is used, which is also developed in-house. The heat conduction, and thermo-elastic capability of AStrO are demonstrated in this work through comparison of results with analytical solutions. The loosely coupled aero-thermo-elastic platform is validated in this work through two applications. In the first application we compare computed solutions for flow over a hypersonic cylindrical leading edge with available experimental data. In the second application we look at solutions for flow over an aerodynamically heated panel.

I. Nomenclature

L	=	objective function
D	=	design variables
u_F	=	state variables from the fluid domain
u_S	=	state variables from the structure domain
T	=	temperature
Q	=	volumetric heat source
k	=	thermal conductivity
c	=	specific heat capacity
H	=	heat transfer coefficient
α	=	thermal diffusivity
ρ	=	density
l	=	length of the geometry
R	=	residual
C	=	viscous damping matrix
M	=	mass matrix
K	=	stiffness matrix
r_0	=	radius of the cylinder
T_0	=	initial temperature
T_b	=	boundary temperature
T_r	=	reference temperature
T_w	=	wall temperature
T_∞	=	free-stream temperature
U_∞	=	free-stream velocity
Ma_∞	=	free-stream Mach number
Re_∞	=	free-stream Reynolds number

[1] PhD Student, Department of Mechanical Engineering, AIAA Member.
[2] Professor, Department of Mechanical Engineering, AIAA Associate Fellow.
[3] PhD Candidate, Department of Mechanical Engineering, AIAA Member.

q_b = boundary heat flux
Bi = Biot number
u = displacement vector in a structure
$\dot{u}$ = velocity vector in a structure
$\ddot{u}$ = acceleration vector in a structure
u_i = nodal displacement solution of a structure under deformation
$\dot{u}_i$ = vector velocity of a point in a structure
$\ddot{u}_i$ = vector acceleration of a point in a structure
n_i = normal vector
t = traction applied over the surface of a structure in vector form
ξ = damping coefficient
σ = stress at a point in a structure in vector form
ϵ = strain at a point in a structure in vector form
C_{ijkl} = elastic stiffness tensor
f = body force per unit volume at a point in a structure in vector form
N_{ij} = matrix of basis functions
Fo = Fourier number
J_0, J_1 = Bessel functions of the first kind

II. Introduction

Numerical analysis has become an important tool in the development of modern aircraft. The use of computational fluid dynamics (CFD) has increased during the last couple of decades, resulting in significant changes to the aerospace design process. Through the use of supercomputers and advanced numerical methods, various aspects of an aerospace vehicle can now be numerically modeled. In this way, costs for design and construction are minimized [1, 2].

The problems at hand often have a multi-physics nature, which requires a coupled simulation [3, 4]. Coupling the codes from the different disciplines allows for each model to provide complementary information to the other, and therefore, eliminates many assumptions. An important example of this type of problem is fluid-structure interaction. In recent years, the development of supercomputers has made simulation of coupled fluid-structure interactions possible. However, in many engineering designs it is not sufficient to just take into account the interaction of the fluid forces and structural deformations; temperature plays an important role as well [5, 6]. Hypersonic vehicles, for example, go through a wide range of flow conditions with large gradients of velocity and temperature close to their surface [7]. One of the major design concerns at these hypersonic velocities are high rates of heat transfer experienced by the vehicle [8]. Therefore, it is essential to account for the effect of temperature in order to obtain accurate numerical simulations [3, 4].

Overall, in order to provide accurate and timely predictions of the coupled responses of integrated interdisciplinary analysis problems, a precise calculation of all the following is required: Aerodynamic loads (aerodynamic pressure and viscous forces), aero-thermal effects (surface heating rate and inner temperature distributions), and structural loads (structural deformation and stresses) [9, 10]. Hence, a coupled aero-thermo-elastic numerical analysis of the problem is vital. The code-coupling can be very challenging in practice. The two main challenges, which arise from the discontinuities between the models, are: time-scale discontinuity, and space-scale discontinuity [4, 11].

One of the most fundamental challenges in computational modeling of aero-thermo-elastic problems is the difference in the time scales between the fluid, thermal and structural disciplines. The fluid problem has the smallest characteristic times, while the thermal time scale is usually much larger than the fluid and structural time scales. Much previous work has assumed a static fluid problem, a quasi-static structural problem, and a transient thermal problem in order to solve this time-scale discontinuity and also to save on computational expense [10, 12].

The discontinuity in the space–scale is also another one of the challenges. In most of these simulations the surface meshes at the interface are non-matching [13]. This is needed for capturing the physics accurately at a reasonable cost on both the fluid and the structure domains [14]. For example, the flow solver usually requires a finer mesh at the boundaries in order to solve for the large velocity gradients present and to be able to capture shock waves and boundary layers. On the other hand, the structure solver requires a finer grid distribution near areas of high curvature [15, 16], but in general employs coarser grid distribution. The use of different types of elements used by different solvers can also cause mesh mismatch at the interface [17]. In such applications the data transfer needs to be as numerically accurate and as physically conservative as possible. Conservation refers to the equilibrium at the boundary, such as

balance of forces or fluxes. When dealing with applications that involve repeated data transfer, achieving both accuracy and conservation is important because errors accumulate over iterations [13].

Generally, when approaching a multidisciplinary simulation, there are two options available: strong and weak coupling. In the first case, the flow, elasticity and heat transfer equations are treated as one single system of equations and solved at once using a single numerical framework. In the second case, the solution of each discipline is obtained from independent codes and then coupled together by exchanging boundary conditions at the interface between the domains [13, 17]. The strong coupling approach is the more stable approach; however, it suffers from the inability to use already available and well-tested solvers. On the other hand, the weak coupling approach is able to use existing, well-developed and tested codes for each discipline. This approach does however have its own disadvantages. These are: the problem of stability and the difficulty of transferring data between the individual disciplinary codes [18, 19].

One way to classify simulation models is to group them into low- or high-fidelity simulations. In many cases when dealing with coupled multidisciplinary simulations, one or more of the disciplines might be solved using low-fidelity models. The premise of the current work is that a modern aero-thermo-elastic capability must include high fidelity models for all the three disciplines. In this work, we solve these models in a weak-coupled fashion in order to take advantage of the already available and well-tested in-house solvers.

This paper is structured as follows. Section III gives more details on the implementation of the aero-thermo-elastic coupling by taking a closer look at each of the required components and the governing equations of each discipline. Section IV provides validation results for the structural solver used in this study. Section V provides validation results for the aero-thermo-elastic analysis capability for two applications: a cylindrical leading edge and an aerodynamically heated panel. Section VI draws conclusions and highlights future work.

III. Aero-Thermo-Elastic Coupling

In this work it was decided to couple the disciplines through a weak coupling approach. This decision was made because it allows us to take advantage of the already available and tested high-fidelity flow solver and structural solver developed in-house for multidisciplinary modeling. Figure 1 illustrates the procedure for the weak coupling strategy we use to solve the aero-thermo-elastic problems presented in this work.

In the rest of this section we look at the different components of the numerical set up required to run an aero-thermo-elastic analysis simulation: the flow solver, the structural solver (elasticity and thermal equation), fluid-structure interaction (FSI) module, and the mesh deformation capability.

A. Flow Solver

The flow solver used in this study is the "Navier-Stokes Unstructured 3D" (NSU3D) code, which is a Reynolds-averaged Navier-Stokes (RANS) solver for unstructured grids [20]. It is a vertex-centered finite volume solver, which is second-order in both time and space. This flow solver uses a line-implicit agglomeration multigrid algorithm, which can be used either as a non-linear solver, or a linear solver within an approximate Newton method, or as a pre-conditioner for GMRES for driving the non-linear steady-state residual to zero [21]. For time-dependent problems, all the above-mentioned solvers can be used in a dual-time stepping approach for solving the non-linear problem, which arises at each time step [22]. NSU3D has been widely validated for both steady state and time-dependent flow problems, having been used in numerous simulations and participations in events such as the Drag Prediction Workshop, the High-Lift Prediction Workshop, and the Aero-elastic Prediction Workshop series [23-26]. More recently, NSU3D has been extended for use in coupled aero-elastic calculations [22, 27, 28]. Detailed explanation of this solver can be found in available previous references [20, 29, 30]. As such, only a concise description of the formulations will be given in this paper.

The flow solver is based on the conservative form of the Navier-Stokes equations. These may be written as:

$$\frac{\partial u(x,t)}{\partial t} + \nabla . F(u) = 0 \tag{1}$$

For moving mesh problems, the above formulation is written in arbitrary Lagrangian-Eulerian (ALE) form, as:

$$\frac{\partial Vu}{\partial t} + \int_{B(t)} [F(u) - \dot{x}u] . n dB = 0 \tag{2}$$

here V refers to the volume of the control volume bounded by a control surface $B(t)$, $\dot{x}$ is the vector of mesh face or edge velocities, and n is the unit normal of the face or edge. Vector u denotes the state vector of conserved variables,

and the flux vector *F* contains both inviscid and viscous fluxes. The equations are closed with the perfect gas equation of state for all cases presented in this work [28, 29].

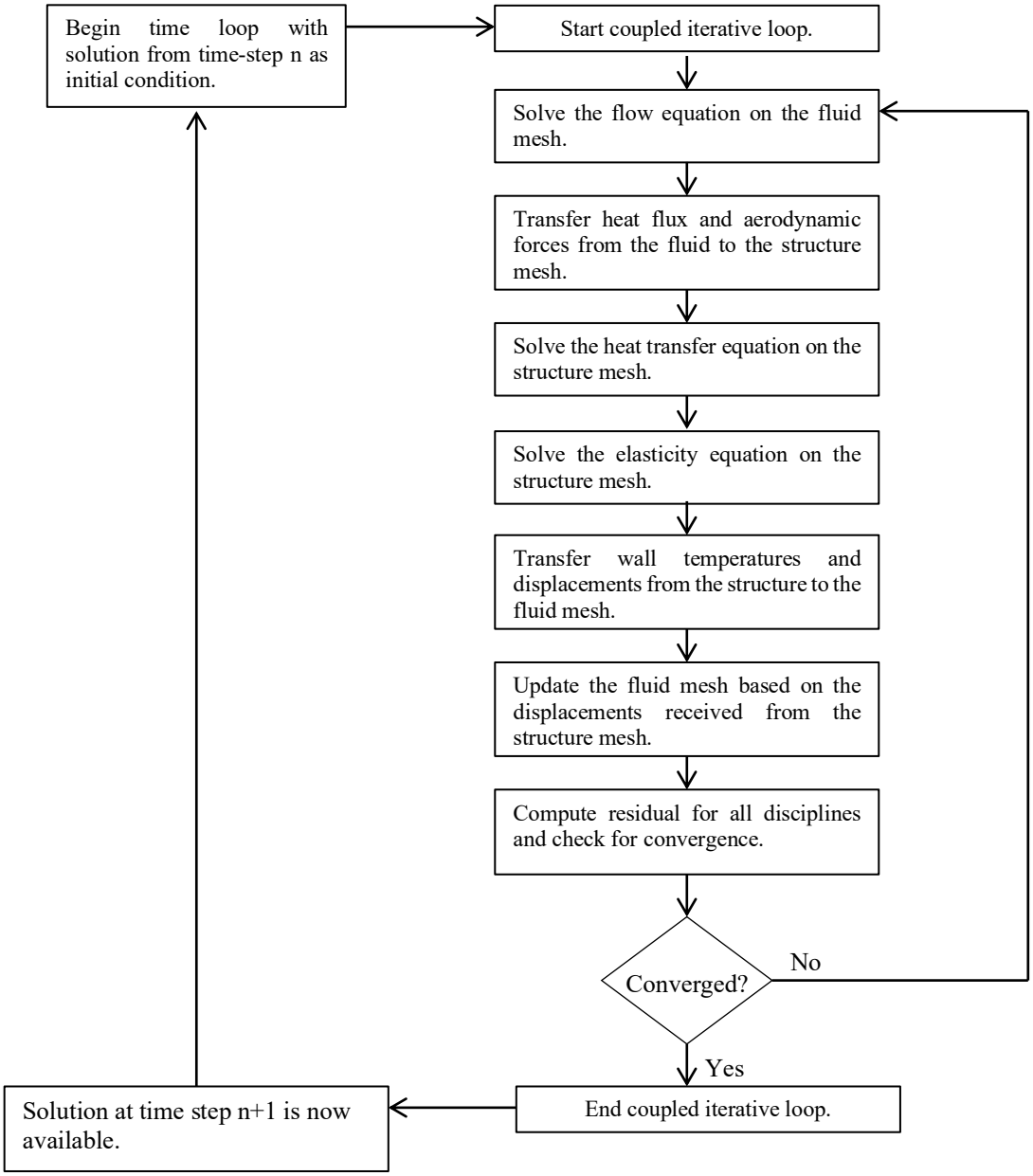

Fig. 1 Iterative loop for advancing from time-step n to time-step n+1 in the aero-thermo-elastic analysis problem with weak coupling.

The time derivative term is discretized using a second-order accurate backward difference formula (BDF2) scheme, leading to the implicit system of equations at each time step given as:

$$\frac{3}{2\Delta t}V^n u^n - \frac{2}{\Delta t}V^{n-1}u^{n-1} + \frac{1}{2\Delta t}V^{n-2}u^{n-2} + S^n(u^n, x^n, \dot{x}^n) = 0 \tag{3}$$

where $V^n = V(x^n)$ represents the mesh control volumes and $S^n(u^n, x^n, \dot{x}^n)$ represents the spatial discretization terms at the n^{th} time step.

The functional dependence of the implicit system to be solved at each time step can be written in residual form as:

$$R^n(u^n, u^{n-1}, u^{n-2}, x^n, x^{n-1}, x^{n-2}) = 0, \quad n = ,2,3, \dots, N \tag{4}$$

where the initial conditions are given by u^0 and x^0, and noting that a BDF1 time discretization is used for the first time step.

At each time step, the implicit residual is solved using a line-implicit solver with agglomeration multigrid. The fluxes are calculated using the Roe scheme [31] and a Barth Jespersen limiter [32] is applied to the cases presented in this work.

B. Structural Solver

The structural solver used in this study is a finite-element solver named AStrO (Adjoint-based Structural Optimizer), which was developed in-house. AStrO has been introduced in previous work [22, 27, 28] and supports both linear and nonlinear finite-element modeling of three-dimensional structures [27]. AStrO also supports finite element modeling of thermo-elastic behavior of structures. AStrO can run static or dynamic analysis of either the heat transfer problem, or the elasticity problem, or the two coupled disciplines [33]. The motivation for constructing an in-house structural solver was to have the capability of doing analysis and calculating sensitivities for coupled CFD and computational thermal and structural dynamics (CTSD) problems [28] .

AStrO is compatible with existing commercial structural analysis software tools such as Abaqus [34]. It contains an interface that can process model input files generated by Abaqus [22]. Dynamic systems are modeled with implicit second-order accurate time integration by the Hilber-Hughes-Taylor "alpha" method [35]. The discretized equations for the elasticity problem are derived from the widely used virtual work formulation [35]. The temperature distribution due to heat conduction through a structure is governed by the Poisson equation, which is discretized in a similar manner as the equations of elasticity. In the following paragraphs we take a closer look at AStrO's governing equations.

The transient elasticity equation solved in AStrO is given as:

$$\nabla \cdot \sigma - \xi \frac{du}{dt} - \rho \frac{d^2u}{dt^2} + f = 0 \tag{5}$$

where f represents the applied body forces, u is the vector of displacements, σ is the stress tensor, and ξ is the damping coefficient.

The principle of virtual work applied to the equations of elasticity for a deformable elastic body subject to applied body forces and surface tractions, as well as damping forces proportional to velocity, can be expressed mathematically as:

$$\int_\Omega (\sigma \cdot \delta\epsilon) d\Omega + \int_\Omega \xi(\dot{u} \cdot \delta u) d\Omega + \int_\Omega \rho(\ddot{u} \cdot \delta u) d\Omega - \int_\Omega (f \cdot \delta u) d\Omega - \int_S (t \cdot \delta u) dS = 0 \tag{6}$$

In the above u, $\dot{u}$, $\ddot{u}$ are the vector displacement, velocity, and acceleration at a point in a structure, σ and ϵ are the stress and strain in second-order tensor form, ξ is the damping coefficient, ρ is the mass density, f is the applied body force per unit volume, t is the applied surface traction per unit area on the structure. The final term is the integral of traction over the surface area of the structure, while all other terms are volume integrals over the body of the structure. The δ operator indicates a variation on the function to its right, meaning the above must hold for any variation of the displacement field u [27, 33]. The virtual displacement, δu, is a function of space throughout the body, and $\delta\epsilon$ is the variation of strain corresponding to that virtual displacement.

The equation of motion for dynamic elastic bodies derived from the principle of virtual work discretized using the finite element method is :

$$\int_\Omega \sigma_i \frac{\partial \epsilon_i}{\partial U_j} d\Omega + \int_\Omega \xi \dot{u}_i N_{ij} d\Omega + \int_\Omega \rho \ddot{u}_i N_{ij} d\Omega - \int_\Omega f_i N_{ij} d\Omega - \int_S t_i N_{ij} dS = 0 \tag{7}$$

where N_{ij} is a matrix of basis functions and U_j is a vector of nodal solution parameters, or degrees of freedom. The matrix equivalent of Eq.(7) is then obtained as shown in Eq.(8):

$$KU + C\dot{U} + M\ddot{U} = F \tag{8}$$

where K is the stiffness matrix, M is the mass matrix, C is the viscous damping matrix, F is the vector of forces, U is the vector of nodal values displacements, $\dot{U}$ vector of nodal values of velocities, and $\ddot{U}$ vector of nodal values of acceleration.

The transient heat equation solved in AStrO is given as:

$$\rho c \frac{\partial T}{\partial t} + \nabla \cdot (k \nabla T) - Q = 0 \tag{9}$$

where, Q is the rate of internal heat generation per unit volume, k is the thermal conductivity, c is the specific heat capacity, ρ the density, and T is the temperature.

The variational form for temperature distribution due to heat conduction in a structure can be developed in a similar fashion as the equations of elasticity:

$$-\int_{\Omega} \left(q \cdot \delta(\nabla T)\right) d\Omega + \int_{\Omega} \rho C_p \dot{T} \delta T d\Omega - \int_{\Omega} Q \delta T d\Omega + \int_{S} (q \cdot n) \delta T dS = 0 \tag{10}$$

The discretized governing equations for heat conduction in structures derived from the variational form using the finite element method is:

$$-\int_{\Omega} q_i \frac{\partial N_j}{\partial x_i} d\Omega + \int_{\Omega} \rho C_p \dot{T} N_j d\Omega - \int_{\Omega} Q N_j d\Omega + \int_{S} q_i n_i N_j dS = 0 \tag{11}$$

where n_i is the normal vector, q_i is the surface heat flux, and N_j the basis function. The matrix equivalent is then obtained as shown in Eq.(12):

$$KT + M\dot{T} = F \tag{12}$$

where T is the nodal values of temperature.

AStrO is capable of modeling the coupled thermo-elastic responses in structures. However, there are several simplifying assumptions made. The first assumption is that thermal material properties such as conductivity and specific heat capacity have no significant dependence on strain. Furthermore, the heat generated by deformation is assumed to be negligible. In other words, the deformation has a one-way dependence on the temperature distribution. These assumptions are acceptable, since the cases to be considered are expected to have small values of strain and within the elastic regime, selected materials will have low internal damping characteristics, and deformation rates will not produce significant heat through phenomena such as viscoelasticity [33].

Under these assumptions, in any given analysis, the temperature distribution of a structure can be obtained first, followed by the deformation solution based on the temperature results in addition to applied loads. To account for the dependence of deformation on the temperature distribution, an adjustment to the definition of total strain is required. Any point in the structure that is subject to a combination of applied stress and change in temperature will exhibit a measure of strain for each of those contributors. Hence, the total strain can be expressed as:

$$\epsilon_i^{total} = \epsilon_i^{stress} + \epsilon_i^{therm} \tag{13}$$

In the governing equations of elasticity based on the principle of virtual work, stress at a point under the assumption of linear elasticity can be expressed as:

$$\sigma_i = C_{ik} \epsilon_k \tag{14}$$

where C_{ik} is the stiffness matrix of the local material. However, ϵ_k in Eq.(14) must only be the strain due to the applied stress. Therefore, in the presence of thermal expansions, we have:

$$\sigma_i = C_{ik} \epsilon_k^{stress} = C_{ik}\left(\epsilon_k^{total} - \epsilon_k^{therm}\right) \tag{15}$$

The strain due to thermal expansion is assumed to be linearly related to temperature, such that the change in temperature from some reference temperature T^{ref} multiplied by a vector of thermal expansion coefficients α gives

the resulting thermal strain to be:

$$\epsilon_k^{therm} = (T - T^{ref})\alpha_k = \Delta T \alpha_k \tag{16}$$

If the stress in Eq.(7) is expressed using Eq.(15) and Eq.(16), then the governing equations for the elastic response taking into account the change in temperature, becomes:

$$\int_\Omega \; C_{ik}\left(\epsilon_k^{total} - \Delta T \alpha_k\right)\frac{\partial \epsilon_i}{\partial U_j} d\Omega + \int_\Omega \; \xi \dot{u}_i \, N_{ij} d\Omega + \int_\Omega \; \rho \ddot{u}_i N_{ij} d\Omega - \int_\Omega \; f_i N_{ij} d\Omega - \int_S \; t_i N_{ij} dS = 0 \tag{17}$$

Since the temperature solution is pre-computed, the effect of thermal expansion shows up as part of the load in the elasticity equations [33].

C. Fluid-Structure Interaction (FSI)

Proper data transfer between different disciplines is one of the most important factors in multidisciplinary analysis and design. Correct modeling of aero-thermo-elastic problems requires an accurate coupling of the fluid and structure codes. Although in these problems the geometry is shared, the models most often have dissimilar meshes. Moreover some of the data from one domain is usually needed to be available on the other domain [36]. The weak coupling method uses an iterative approach to calculate the same temperature and heat flux at the boundaries of the fluid and structure domain. Likewise, it checks to see if the values for the aerodynamic loads on the fluid side and the displacements generated by the structure solver in response to these aerodynamic loads, have converged. The computation alternates between the fluid and structure domains with exchange of the above-mentioned boundary conditions [15, 16]. In weak coupled codes, the CFD and CTSD codes are alternatively called from a master program. This master program is also in charge of transferring data between the codes on the CFD/CTSD interface.

In order to control the stability and convergence in these problems, the choice of the boundary condition is very important. In the literature, the continuity of temperature and heat flux at the interface is mainly implemented by imposing the wall temperature distribution computed from the CTSD solution on the fluid side and the heat flux distribution computed from the CFD solution on the structure side. This method is known as the flux forward temperature back (FFTB) method or the Dirichlet-Neumann boundary condition. Many researchers have shown that the use of this type of boundary condition is the key to achieving numerical stability and having robust convergence [15, 16, 37, 38].

An FSI module had previously been created in-house and used for aero-elastic analysis and design [22, 28]. This model was able to successfully transfer the aerodynamic forces from the fluid solver to the structure solver, and in return pass the calculated displacements to the fluid surface mesh [22]. This module was updated so that it can also transfer temperature and heat flux between the fluid and structure meshes. When dealing with the aero-thermo-elastic analysis, we need to exchange the aerodynamic forces and heat fluxes from the fluid domain to the structure domain, and in return send the temperatures and displacements from the structure mesh to the fluid mesh. The effects of the temperature on the structure are dealt with internally in the structure code as explained in the previous section.

In practice the FSI computes the heat fluxes and the aerodynamic forces at each CFD surface mesh point. These values are then projected onto the finite-element basis functions where they are assembled in the form of heat fluxes and forces on the finite-element nodal locations. Conversely, once the structural temperature and displacement solutions have been computed, they are transferred back to the surface CFD mesh in a similar manner [28]. This transfer of data between the two meshes can be summarized with the following equations:

$$\begin{cases} \mathrm{Q_{CTSD}} = [\mathrm{P}]\mathrm{Q_{CFD}} \\ \mathrm{T_{CFD}} = [\mathrm{P}]^{\mathrm{T}}\mathrm{T_{CTSD}} \end{cases} \tag{18}$$

$$\begin{cases} \mathrm{F_{CTSD}} = [\mathrm{P}]\mathrm{F_{CFD}} \\ \mathrm{U_{CFD}} = [\mathrm{P}]^{\mathrm{T}}\mathrm{U_{CTSD}} \end{cases} \tag{19}$$

where [P] represents the rectangular transfer matrix which projects pointwise CFD surface heat fluxes and forces onto the individual structure mesh surface points. The transpose of the matrix is used to obtain the CFD surface temperatures and displacements from the structure mesh [22]. The interpolation patterns which define the [P] matrix are computed by locating the perpendicular projection of each point of the surface CFD mesh on the structure model elements [28]. This is done through a fast parallel search technique, which is based on the minimum distance search [39].

It should be mentioned here that the in-house developed FSI is capable of working with non-matching fluid and structure meshes with different element types and mesh resolution. Moreover, the developed FSI has the ability to handle fluid and structure models that have non-matching outer-mold line (OML) geometries [22]. Additionally, the FSI formulation is discretely conservative for the transfer of forces and heat fluxes from the fluid to the structure and satisfies the principle of conservation of virtual work for the transfer of displacements from the structure to the fluid.

D. Mesh Deformation

When dealing with aero-thermo-elastic problems, we require a mesh deformation capability in order to account for the displacements computed by the structural solver in response to the aerodynamic and thermal loads. When running time-dependent problems, we may also have prescribed surface deflections at certain times, such as when simulating prescribed motion of a control surface. Hence, the CFD solver needs to be modified to take into account the additional dynamics introduced due to the mesh motion, and the fluid equations must be written in the ALE framework [12, 40]. NSU3D employs a discretization that respects the Geometric Conservation Law (GCL) [41] to make sure the flow solver keeps its accuracy and stability in the presence of arbitrary mesh motion. Significant work has been done in the past on the development of a robust and efficient mesh deformation technique [42, 43]. This approach is based on the linear elasticity model and the mesh deformation equations are discretized using a second-order accurate continuous Galerkin finite-element approach [22]. The equations for the mesh deformation are solved using the same line-implicit multigrid algorithm used for solving the flow equations [25].

IV. Structure Solver Validation

AStrO has been validated by performing unit tests on each element type and comparing results either with analytical solutions when available, or with solutions generated by Abaqus [22, 33]. In the following we first present results for the validation of the heat conduction solution capability. Next, we present two validation cases for the thermo-elastic capability. This verification was required before moving on to coupling the fluid solver with the structure solver. The elastic and aero-elastic capabilities have been demonstrated in previous work [22, 27, 28, 33].

A. Thermal Solver Validation

In the following some tests that were used to validate the heat conduction capability in AStrO are presented. The temperature solutions calculated by AStrO are compared against analytical solutions. We look at transient cases involving one-dimensional and two-dimensional heat conduction. In this section we have used the same validation problems presented in reference [7].

The properties of the material for all the cases presented in this section are given in Table 1. The transient heat equation is Eq. (9) from the previous section, and for these cases we are assuming the volumetric heat source Q to be zero.

We have taken into account four different transient cases for this validation study. For the first three cases, the geometry used is a three-dimensional cube with a length of $0.01m$ in the x-, y-, and z-directions. The mesh used for the cube has 9,261 nodes and 8,000 linear hexahedral elements. For the last transient case we consider a quarter cylinder geometry. The quarter cylinder mesh has 14,535 nodes and 12,800 linear hexahedral elements. In the following we look at each case and compare the computational temperature solutions with the analytical solutions. Please refer to Table 1 for all the material properties in the cases discussed in the coming pages.

Table 1 Material properties and details of the geometry for the transient heat conduction cases [7].

Property	***Value***
Initial temperature (T_0)	300 K
Length of bar *(l)*	0.01 m
Thermal conductivity *(k)*	10 W/(m.K)
Density *(ρ)*	8000 kg/m^3
Specific heat capacity *(C)*	500 J/(kg.K)
Thermal diffusivity (α)	2.5×10^{-6} (m^2/s)
Heat transfer coefficient *(H)*	1000 W/(m^2.K)

1) Transient Heat Conduction with Dirichlet Boundary Condition and Constant Thermal Properties, in a Cube

For this first case, we consider heat conduction in one dimension with constant thermal properties. A Dirichlet boundary condition is applied at x = $0.01m$ with a fixed uniform temperature of $T_D = 500K$. The analytical solution is obtained from Eq. (20) [7, 44].

$$\frac{T(x,t)-T_0}{T_D-T_0} = 1 - \frac{4}{\pi}\sum_{n=0}^{\infty}\frac{(-1)^n}{2n+1}\exp\left(\frac{-(2n+1)^2\pi^2}{4}\cdot\frac{at}{l^2}\right)\cos\left(\frac{(2n+1)\pi}{2}\cdot\frac{x}{l}\right) \quad (20)$$

Figure 2 shows a comparison of the temperature solution for both the analytical and computational methods at different time instances for different x locations in the cube. As can be seen the computational results agree well with the analytical solution.

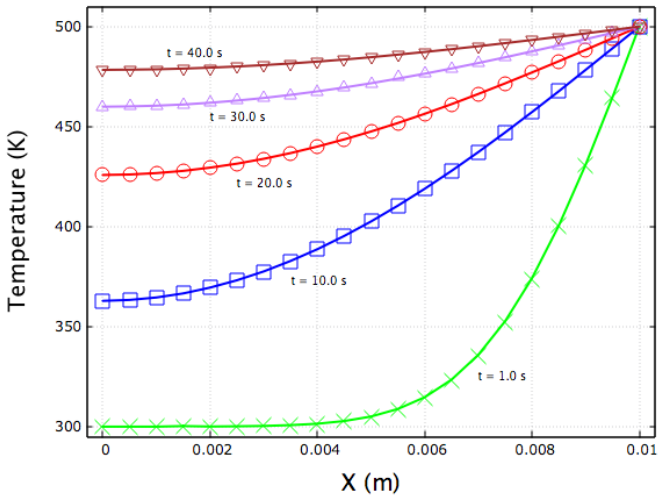

Fig. 2 Comparison of the temperature distribution from AStrO with analytical solution for the case of transient heat conduction with Dirichlet boundary condition and constant thermal properties, in a cube.

2) Transient Heat Conduction with Neumann Boundary Condition and Constant Thermal Properties in a Cube

In this second case, instead of applying a Dirichlet boundary condition to one side of the cube as was done in the previous case, we apply a Neumann boundary condition. A constant heat flux of $q_b = 7.5 \times 10^5\ W/m^2$ is applied at x = $0.01m$. Again, we are assuming constant thermal properties. The computational solution is compared with the analytical solution obtained from Eq. (21) [7, 45].

$$\frac{T(x,t)-T_0}{q_b l/k} = \frac{at}{l^2} + \frac{1}{3} - \frac{x}{l} + \frac{1}{2}\left(\frac{x}{l}\right)^2 - \frac{2}{\pi^2}\sum_{n=1}^{\infty}\frac{1}{n^2}\exp\left(-n^2\pi^2\frac{at}{l^2}\right)\cos\left(n\pi\frac{x}{l}\right) \quad (21)$$

The computational results for the temperature distribution along the length of the cube at t = 4s are shown in Fig. 3 and Fig. 4.

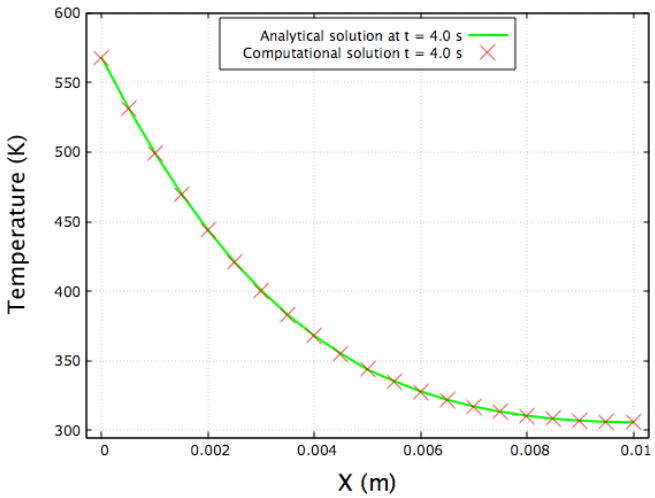

Fig. 3 Comparison of the temperature distribution from AStrO with analytical solution for the case of transient heat conduction with Neumann boundary condition and constant thermal properties, in a cube at t = 4s.

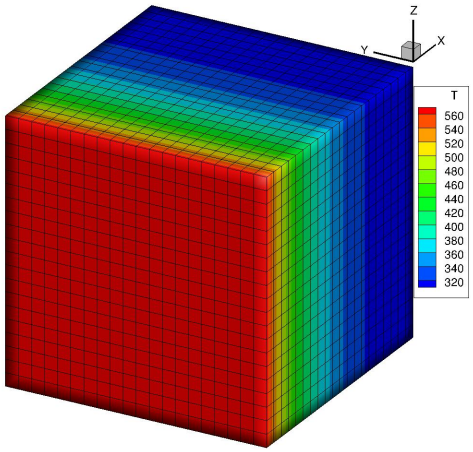

Fig. 4 Temperature distribution from AStrO for the case of transient heat conduction with Neumann boundary condition and constant thermal properties, in a cube at t = 4s.

3) Transient Heat Conduction with Neumann Boundary Condition and Variable Thermal Properties in a Cube

Here, we assume the same problem as the previous section, however, now we have variable thermal properties: $\kappa = k(T)$ and $c = C(T)$. Hence, we still have a one-dimensional heat conduction problem in a three-dimensional cube with a Neumann boundary condition at x = 0.01m. However, the values of κ, c, and α all change with changes in temperature as shown in Eq. (22), Eq. (23), and Eq. (24) respectively:

$$k(T) = k_1 + \frac{k_2 - k_1}{T_2 - T_1}(T - T_1) \tag{22}$$

$$\mathrm{C(T)} = \mathrm{C_1} + \frac{\mathrm{C_2} - \mathrm{C_1}}{\mathrm{T_2} - \mathrm{T_1}}(\mathrm{T} - \mathrm{T_1}) \tag{23}$$

$$\alpha = \frac{k_1}{\rho C_1} = \frac{k_2}{\rho C_2} = \frac{k(T)}{\rho C(T)} \tag{24}$$

The analytical solution for this specific problem is obtained through the use of Eq. (25) [7, 46].

$$\frac{\theta(x,t) - \theta_0}{q_b l/k} = \frac{at}{l^2} + \frac{1}{3} - \frac{x}{l} + \frac{1}{2}\left(\frac{x}{l}\right)^2 - \frac{2}{\pi^2}\sum_{n=1}^{\infty}\frac{1}{n^2}\exp\left(-n^2\pi^2\frac{at}{l^2}\right)\cos\left(n\pi\frac{x}{l}\right) \tag{25}$$

where:

$$\theta_0 = (T_0 - T_1) + \frac{k_2 - k_1}{T_2 - T_1}\frac{1}{2k_1}(T_0 - T_1)^2\,, \theta = (T - T_1) + \frac{k_2 - k_1}{T_2 - T_1}\frac{1}{2k_1}(T - T_1)^2 \tag{26}$$

The values of the thermal properties used in this problem can be found in Table 1 presented previously and Table 2 shown here.

Table 2 Variable thermal properties for the cube [7].

$T\,(K)$	$K\,(w/m.K)$	$C\,(J/kg.K)$
$T_1 = 300$	$K_1 = 10$	$C_1 = 500$
$T_2 = 1300$	$K_2 = 100$	$C_2 = 5000$

Figure 5 provides a comparison of the analytical and computational temperature solution along the length of the cube at t = 4s. As can be seen the numerical solution follows the analytical solution very closely. The temperature distribution as calculated by AStrO is shown in Fig. 6.

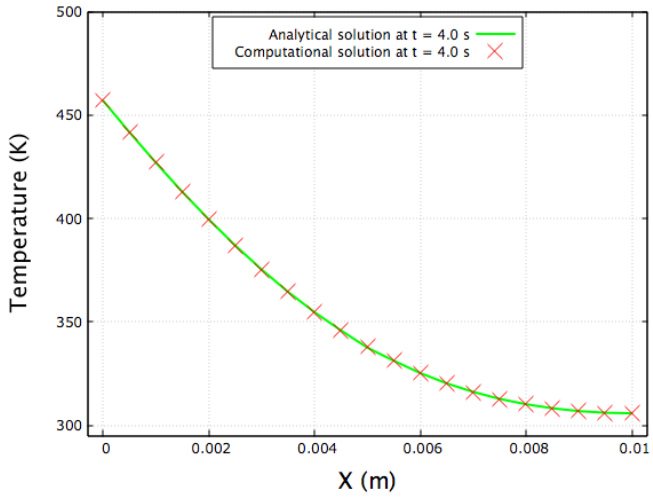

Fig. 5 Comparison of the temperature distribution from AStrO with analytical solution for the case of transient heat conduction with Neumann boundary condition and variable thermal properties in a cube.

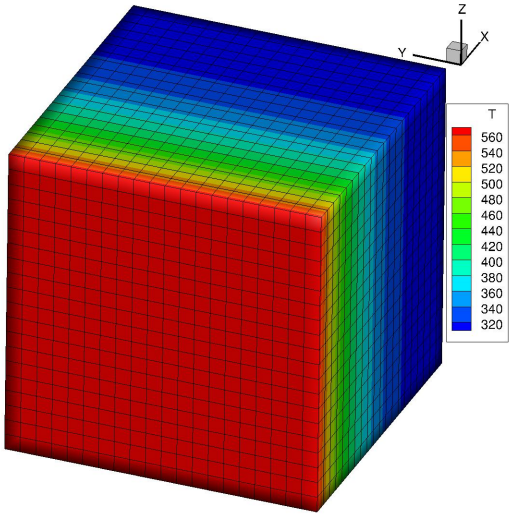

Fig. 6 Temperature distribution from AStrO for the case of transient heat conduction with Neumann boundary condition and variable thermal properties, in a cube at t = 4s.

4) Transient Heat Conduction with Perfect Gas Convection on a Cylinder

In the previous sections we looked at one-dimensional heat conduction problems. In this section, we consider a heat conduction problem in two-dimensions. Here we study heat conduction in a quarter cylinder. A Neumann boundary condition is prescribed by perfect gas convection at the locations where the radius of the cylinder is $r_0 = 0.01m$. For this case we have a variable heat flux applied and this value is updated by the wall temperature through Eq. (27) as:

$$q_b = -H(T_r - T_W) \tag{27}$$

where H is the heat transfer coefficient, T_W is the wall temperature, and T_r is the reference temperature which for this problem is taken as $T_r = 1300K$. As mentioned before, T_W is not constant and changes with time, and hence so does the value of q_b.

Assuming constant thermal properties in this case, the analytical solution is given by Eq. (28) [7, 47].

$$\frac{T(r,t)-T_r}{T_0-T_r} = \sum_{n=1}^{\infty} k_n J_0\left(b_n \frac{r}{r_0}\right) exp\left(-b_n^2 Fo\right) \tag{28}$$

where:

$$k_n = \frac{2Bi}{(b_n^2+Bi^2)J_0(b_n)}\ , \quad Bi = \frac{Hr_0}{k}\ , \ Fo = \frac{at}{r_0^2} \tag{29}$$

In the above equations, the characteristic values b_n are the roots of the equation:

$$b_n J_1(b_n) = BiJ_0(b_n) \tag{30}$$

J_0 and J_1 are the Bessel functions of the first kind. In the above equation Bi and Fo are the Biot and Fourier numbers. Figures 7 and 8 show the temperature distribution along the radius of the cylinder at t = 5*s*. The numerical solution from AStrO is shown to compare well with the analytical solution in Fig. 7.

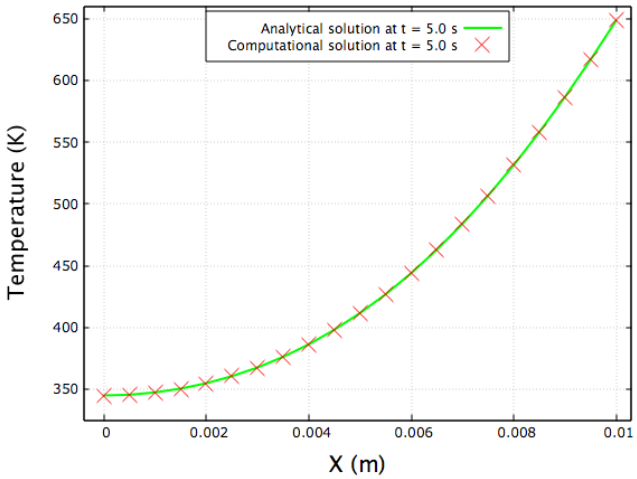

Fig. 7 Comparison of the temperature distribution from AStrO with analytical solution for the case of transient heat conduction with perfect gas convection on a quarter cylinder at t = 5s.

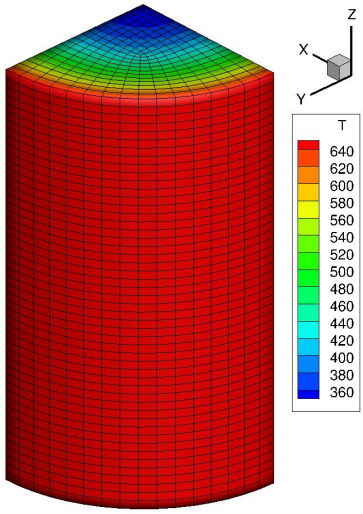

Fig. 8 Temperature distribution from AStrO for the case of transient heat conduction with perfect gas convection on a quarter cylinder at t = 5s.

B. Thermo-Elastic Validation

This section provides a demonstration of the coupled thermo-elastic modeling capability of AStrO. We look at two cases and compare simulation results with the available analytical solutions.

1) Thermo-Elastic Study of a Solid Cube with Applied Thermal Load

We developed this first case in order to test AStrO's ability to couple thermal loads from the thermal solver with the structural solver. For this case the geometry used is a three-dimensional cube with a length of $1m$ in the x-, y-, and z-directions. There are no mechanical loads applied, and we look at the effect of the thermal load on the cube. The elastic material properties of the cube were set to be fully isotropic, and the material properties are presented in Table 3.

Table 3 Solid cube material properties.

Property	***Value***
Thermal Conductivity *(k)*	1.0 *W/(m.K)*
Thermal expansion (α)	10^{-4} *1/K*
Modulus of elasticity (E)	10^{6} *N/m²*
Poisson's ration (ν)	0.3 (dimensionless)

The governing partial differential equations for the thermal and elastic response of a solid body in static equilibrium, are:

$$\frac{\partial q_i}{\partial x_i} - Q = 0 \tag{31}$$

$$\frac{\partial \sigma_{ij}}{\partial x_j} + f_i = 0 \tag{32}$$

If we assume the elastic body is only subject to thermal loads, the governing equations for elastic responses simplifies to:

$$\frac{\partial \sigma_{ij}}{\partial x_j} = 0 \tag{33}$$

In Eq.(34) stress is computed from the combination of total strain and strain due to thermal expansion:

$$C_{ijkl}\left(\frac{\partial \epsilon_{kl}^{total}}{\partial x_j} - \alpha \frac{\partial T}{\partial x_j}\right) = 0 \tag{34}$$

Equation (34) provides a relationship between strain and temperature in the absence of applied mechanical loads. where C_{ijkl} is the elastic stiffness tensor and α is the thermal expansion coefficient. In this problem we assume these two variables to be constant through the elastic body. Also, the assumption of isotropic material properties further simplifies C_{ijkl} due to symmetry.

The strategy in this test is to choose analytical displacement and strain fields within the cube and then derive the corresponding temperature distribution based on Eq.(34). Then the internal heat generation field can be found from Eq.(31). The derived loading and boundary conditions can be applied to the finite element model in AStrO. The simulated temperature and displacement from AStrO, can then be compared with the analytical solution.

Description of the Solid Cube Case Computational Set-Up

Here, we define an analytical displacement and strain field and then derive the analytical equations for the temperature distribution, internal heat generation and heat flux. The analytical internal heat generation and heat flux are used as applied load and boundary condition on the solid cube model run with AStrO.

The analytical displacement field within the cube is defined as follows:

$$\begin{cases} u_1 = (\frac{1}{3}x_1^3 + x_2^2 + x_3^2) \times 10^{-3} \\ u_2 = (x_1^2 + \frac{1}{3}x_2^3 + x_3^2) \times 10^{-3} \\ u_3 = \left(x_1^2 + x_2^2 + \frac{1}{3}x_3^3\right) \times 10^{-3} \end{cases} \tag{35}$$

In this case a linear geometry is assumed so that the total strain field can be expressed as:

$$\begin{cases} \epsilon_1 = \frac{\partial u_1}{\partial x_1} = x_1^2 \times 10^{-3} \\ \epsilon_2 = \frac{\partial u_2}{\partial x_2} = x_2^2 \times 10^{-3} \\ \epsilon_3 = \frac{\partial u_3}{\partial x_3} = x_3^2 \times 10^{-3} \\ \gamma_{12} = \frac{\partial u_1}{\partial x_2} + \frac{\partial u_2}{\partial x_1} = 2 \times 10^{-3}(x_1 + x_2) \\ \gamma_{13} = \frac{\partial u_1}{\partial x_3} + \frac{\partial u_3}{\partial x_1} = 2 \times 10^{-3}(x_1 + x_3) \\ \gamma_{23} = \frac{\partial u_2}{\partial x_3} + \frac{\partial u_3}{\partial x_2} = 2 \times 10^{-3}(x_2 + x_3) \end{cases} \tag{36}$$

From the above the expression for the temperature field is found to be :

$$T = \frac{2\times10^{-3}}{\alpha^{TE}}\left[\frac{\left(\frac{1}{2}C_{11}x_1+C_{44}+C_{55}\right)}{(C_{11}+C_{12}+C_{13})}x_1 + \frac{\left(\frac{1}{2}C_{22}x_2+C_{44}+C_{66}\right)}{(C_{21}+C_{22}+C_{23})}x_2 + \frac{\left(\frac{1}{2}C_{33}x_3+C_{55}+C_{66}\right)}{(C_{31}+C_{32}+C_{33})}x_3\right] \tag{37}$$

With isotropic thermal conductivity, the heat flux can be written as:

$$q_i = -k\frac{\partial T}{\partial x_i} = \frac{2\times10^{-3}}{\alpha^{TE}}\left[\frac{(C_{11}x_1+C_{44}+C_{55})}{(C_{11}+C_{12}+C_{13})}, \frac{(C_{22}x_2+C_{44}+C_{66})}{(C_{21}+C_{22}+C_{23})}, \frac{(C_{33}x_3+C_{55}+C_{66})}{(C_{31}+C_{32}+C_{33})}\right] \tag{38}$$

Finally, the internal heat generation field is:

$$Q = \frac{\partial q_i}{\partial x_i} = \frac{2\times10^{-3}}{\alpha^{TE}}\left[\frac{C_{11}}{(C_{11}+C_{12}+C_{13})} + \frac{C_{22}}{(C_{21}+C_{22}+C_{23})} + \frac{C_{33}}{(C_{31}+C_{32}+C_{33})}\right] \tag{39}$$

By applying Eq.(38) and Eq.(39) as thermal surface flux and heat generation loads to the finite element model of the solid cube, the analytical temperature distribution of Eq.(37) , and subsequently the original displacement and strain field of Eq.(35) and Eq.(36) can be recovered from AStrO.

Numerical Results for the Thermo-Elastic Analysis of the Solid Cube Case

A convergence study was done in order to validate the strain, displacement and temperature results simulated by AStrO. We took into account models of the solid cube at four levels of mesh refinement. The nominal element size Δx at each progressive refinement level were set to 1/4, 1/8, 1/16, and 1/32 meters. The models were all constructed using linear hexahedral elements. The root mean square of error in temperature, displacement and strain for the increasing mesh refinements are computed using the following equation:

$$RMS(error) = \sqrt{\frac{\sum_{i=1}^{n_{els}}(U_i^{FE} - U_i^{exact})^2(Vol_i)}{Total\ Volume}} \tag{40}$$

The convergence of the solution with mesh refinement is demonstrated in Fig. 9 through Fig. 11. All quantities are computed at the centroid of each element. All solutions asymptotically converge to the exact solution with increasing mesh refinement at a logarithmic slope of roughly two, which is to be expected for linear elements.

Figures 12 and 13 show plots of the resulting temperature and displacement distribution under the specific loading described above as computed by AStrO for the mesh at refinement level three.

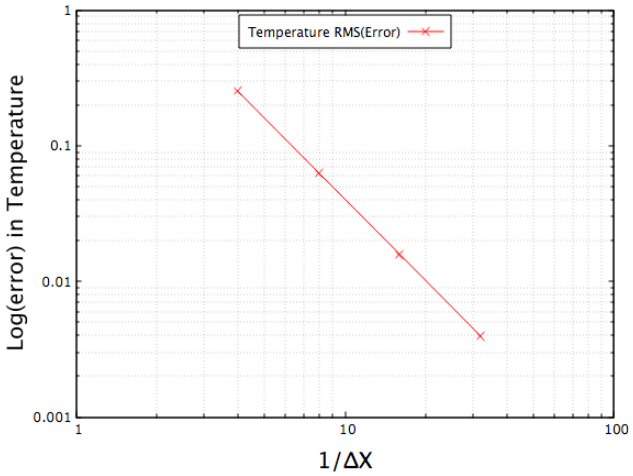

Fig. 9 Error convergence of the temperature solution in the solid block.

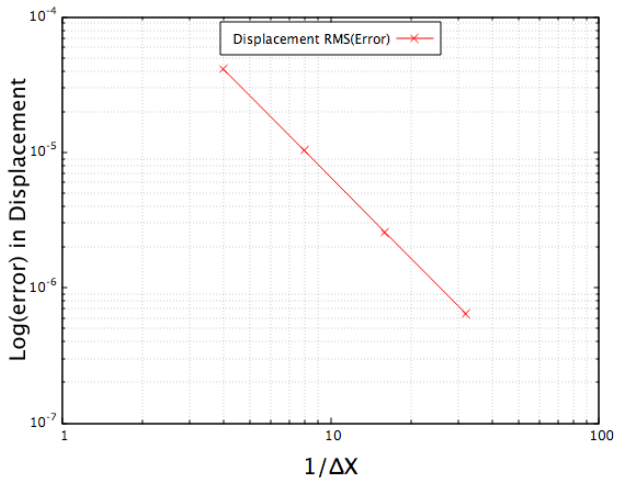

Fig. 10 Error convergence of the displacement solution in the solid block.

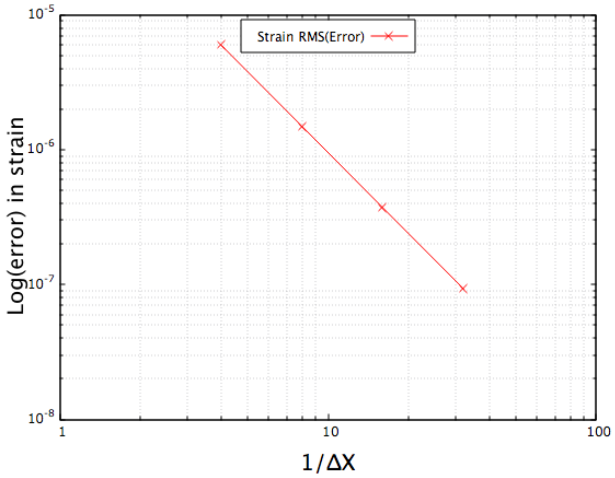

Fig. 11 Error convergence of the strain solution in the solid block.

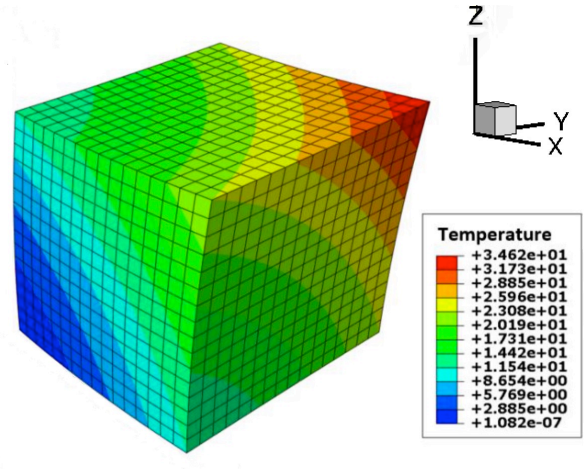

Fig. 12 Distribution of temperature in the solid block at refinement level three obtained from AStrO.

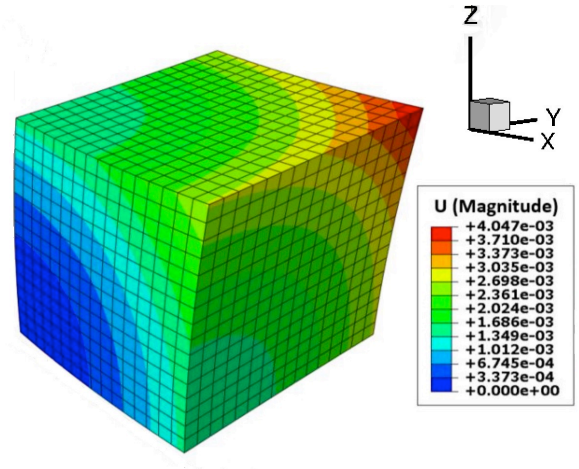

Fig. 13 Distribution of the displacement magnitude in the solid block at refinement level three obtained from AStrO.

2) Thermo-Elastic Study of a Heated Panel

As mentioned previously, the fluid/thermal/structural interactions play an important role in many design problems. One such problem is the thermal protection systems on hypersonic flight vehicles. The study of aerodynamically heated panels is a preliminary but important step towards the objectives of analyzing more realistic material and structures for such vehicles [48]. With this in mind, a study was done on an aerodynamically heated panel in order to validate AStrO's thermo-elastic analysis capability. We consider the case of a thin panel subjected to aerodynamic heating. This test case was first studied in reference [49] to test the aero-thermo-elastic analysis problem. However, a simplified analytical solution to this problem was given in reference [50] which can also be used to verify the thermo-elastic numerical solution for the early time steps.

Description of the Heated Panel Case Computational Set-Up

A schematic of the computational model and boundary conditions for this problem is shown in Fig. 14. The panel is supported by immovable supports on the left and right edges of the bottom surface. The bottom surface of the panel is insulated, while the faces on the right and left side of the panel have a constant temperature equal to the initial temperature of 530*R*. A uniform heat flux is applied to the top surface of the panel. Under these thermal and structural boundary conditions, the panel deforms into a convex shape [48-50].

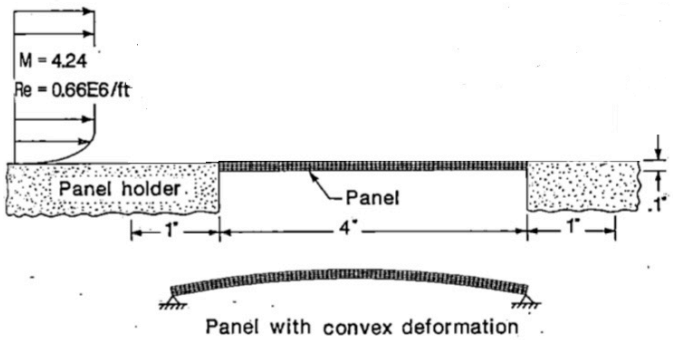

Fig. 14 Coupled thermal/structural model and boundary conditions for a heated flat plate reproduced from reference [50].

The test panel is 4*in* long, has a thickness of 0.1*in*, and a width of 0.5*in.* It is made from AM-350 stainless steel. The properties for the panel are tabulated in Table 4 [50].

Table 4 Panel material properties [50].

Property	***Value***
Density *(ρ)*	0.282 lbm/in^3
Thermal Conductivity *(k)*	0.12864×10^{-3} *BTU/(s.in.R)*
Specific heat capacity *(C)*	0.11162 *BTU/(lbm.R)*
Thermal expansion (α)	0.62643×10^{-5} *1/R*
Modulus of elasticity (*E*)	0.35346×10^{8} lbf/in^2
Poisson's ration (v)	0.25 (dimensionless)

At these early times, the heating rate across the panel is nearly uniform, and can be approximated by the following equation [50]:

$$\dot{q}(t) = 0.026 - 0.0001t \ (\frac{BTU}{in^2.s}) \tag{41}$$

Equation (41) is used as a thermal boundary condition in order to mimic the aerodynamic heating for the thermo-elastic validation.

At early times, panel temperatures may be estimated by assuming, 1) that energy losses at panel supports are negligible, 2) that radiation energy losses are negligible as a result of low panel temperature, 3) that no panel thickness temperature gradient is permissible for the thin stainless-steel panel. With these assumptions in mind the average panel temperature can be calculated through the following equation [50]:

$$T_a(t) = \frac{1}{\rho ch} \cdot (0.026t - 0.00005t^2) + T_0 \tag{42}$$

where T_0 is the initial panel temperature.

The panel's structural response at early times can be approximated using the beam-column theory. In this theory we assume that deformations are small, shear effects are neglected, and, for cylindrical bending, the beam's flexural rigidity is $D = Eh^3/12(1-\upsilon^2)$, where E is the modulus of elasticity and υ is the Poisson's ratio. Hence, the panel deflection is approximated with the following [50]:

$$v(x) = (^h/_2)(\cos \lambda x/2 - 1) \tag{43}$$

where $\lambda = \sqrt{P/D}$, and the axial constraint force P is computed from [50]:

$$\frac{Pl}{hE} + \frac{h^2}{2}\lambda \tan\left(\frac{\lambda l}{2}\right) + \frac{h^2}{8}\frac{P}{D} \times \frac{l}{2} - \frac{sin\lambda l}{2\lambda}/cos^2\frac{\lambda l}{2} - \alpha \Delta T l = 0 \tag{44}$$

where $\Delta T = T_a - T_0$.

The panel stresses according to beam-column theory are:

$$\sigma_x = -\frac{P}{h} + \frac{6P}{h^2}\frac{\cos(\lambda x)}{\cos(l/2)}y \qquad (45)$$

In the following section we will use the analytical results from Eq.(42), Eq.(43) and Eq.(45) to validate the results from AStrO for the heated panel case.

Numerical Results for the thermo-elastic Analysis of the Heated Panel Case

Here, we present the numerical results for the thermo-elastic analysis of the heated panel problem described above. The panel deformations were computed three times at 10s intervals for a test duration of 30*s*. Two meshes have been used in this study. The coarse mesh has 3,216 nodes, and 1,995 hexahedral elements. The fine mesh has 15,960 nodes and 11,925 hexahedral elements. The results for the temperature, maximum deformations and stresses are shown in Table 5, Table 6, and Table 7 respectively. The time step used for the coupled thermo-elastic analysis was 0.01*s*. Hence 3000 time-steps were required to heat the panel for 30*s*. As can be seen, the computed results are very close to the analytical solutions. The computed results are not exactly the same as the analytical solutions because as explained earlier, the analytical equations themselves involve various assumptions. The computed results from reference [50] also have small variation with respect to the analytical solutions.

Table 5 Panel temperature solution *T (l/2, t)* in Rankine.

Time(s)	*Computational solution*		*Analytical solution*
	Coarse mesh	*Fine mesh*	
10	610.997	610.996	606.22
20	688.8299	688.8289	685.31
30	763.4818	763.395	767.28

Table 6 Panel deformation *v (l/2, t)* in inches.

Time(s)	*Computational solution*		*Analytical solution*
	Coarse mesh	*Fine mesh*	
10	0.0138	0.0136	0.0127
20	0.0262	0.0259	0.0234
30	0.0374	0.0370	0.0336

Table 7 Panel stresses σ_x *(l/2,-h/2, t)* in ksi.

Time(s)	*Computational solution*		*Analytical solution*
	Coarse mesh	*Fine mesh*	
10	- 12.223	- 13.588	- 13.2
20	- 23.136	- 25.721	- 24.0
30	- 33.060	- 35.064	- 34.3

Contours of the displacements in the x- and y-directions for the coarse mesh are shown in Fig. 15. The contours clearly show the convex deformations in the panel.

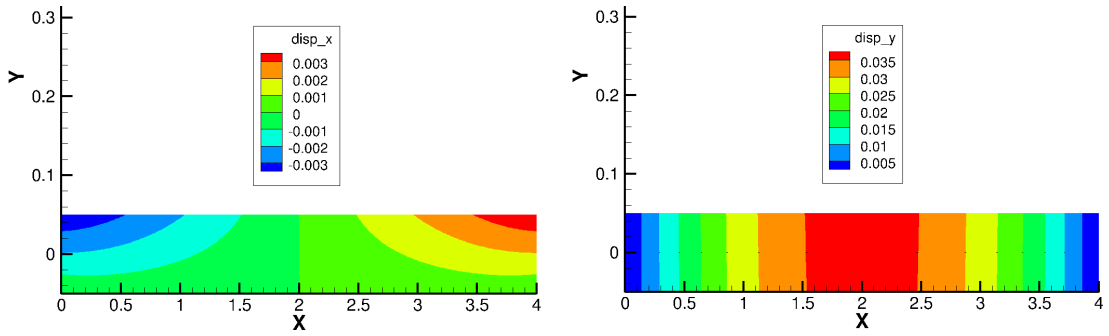

Fig. 15 Contour of the panel displacement in the x- and y- direction at t = 30s as calculated by AStrO.

V. Aero-Thermo-Elastic Analysis Capability Validation

As mentioned before, the flow solver NSU3D and AStrO's elasticity capability have been validated in many previous works [21-28]. The aero-elastic coupling of NSU3D and AStrO have also been studied formerly [22, 27, 28]. In the previous sections of this work, we showed validation results for the thermal and thermo-elastic capabilities of AStrO. Now that we have validated and tested solvers for each discipline, and we also have validation results for the aero-elastic and thermo-elastic capabilities, we can move on to validating the aero-thermo-elastic analysis capability. When an aircraft operates at high speeds, its aeroelastic behavior will be affected by aerodynamic heating and vice versa. Hence, we look at two applications for hypersonic flows: hypersonic flow over a cylindrical leading edge, and an aerodynamically heated panel.

A. Hypersonic Flow Over a Cylindrical Leading Edge

Leading edges of hypersonic vehicles experience intense stagnation point pressures and heating rates. This severe temperature levels and gradients pose a great challenge to the designer [9]. Hence, it is of great importance to study the aero-thermo-elastic analysis of hypersonic flow over leading edges. For these reasons, we study the fluid-thermal-structural behavior of an aerodynamically heated cylindrical leading edge. The coupled analysis is applied to a three-dimensional cylinder as was studied experimentally in reference [51]. These experimental results have been used frequently in the past for validation of aero-thermo and aero-thermo-elastic coupling approaches [9, 10, 52, 53].

In the following, we first look at an overview of the wind tunnel experiment. Next, a brief description of the fluid and structure meshes used in this numerical study is given. Finally, we present numerical results for the predicted pressure, wall heating-rates, temperature distribution, and stresses. These results are compared with the experimental data [51] and previous work [9, 10, 52, 53] for validation.

1) An Overview of the Wind Tunnel Experiment

The solution for Mach 6.47 flow over a cylinder is used to demonstrate and validate the integrated flow-thermal-structural analysis approach. A schematic of the experiment performed in 1987 by Allan Wieting [51] in the NASA Langley 8-foot High Temperature Tunnel is shown in Fig. 16. The initial free-stream flow parameters are summarized in Table 8. The length, diameter, and thickness of the cylinder used are: $0.1143m$, $0.0762m$, and $0.0127m$, respectively. The material properties of stainless steel 321 used for the cylinder are shown in Table 9. Approximately fifty pressure taps, and coaxial thermocouples were placed circumferentially along the cylinder surface to allow the accurate measurement of the aerodynamic pressure and heating rate distribution. More details regarding the experimental configuration, flow conditions and results can be found in reference [51].

Table 8 Initial free-stream conditions for the flow [51].

Free-stream conditions	***Value***
Free-stream Mach number (Ma_∞)	6.47 (dimensionless)
Wall temperature (T_w)	294.4 K
Free-stream Reynolds number (Re_∞)	1.312×10^6 $1/m$
Free-stream temperature (T_∞)	241.5 K
Free-stream velocity (U_∞)	2015.43 m/s
Free-stream pressure (P_∞)	648.1 Pa

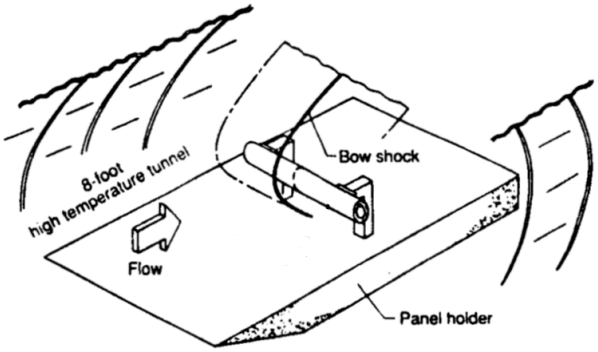

Fig. 16 Experimental configuration for flow over a cylinder in the 8-Foot High Temperature Tunnel reproduced from reference [9].

Table 9 Material properties of 321 stainless steel at 400*K* [52].

Property	*Value*
Density *(ρ)*	8030 kg/m^3
Thermal Conductivity *(k)*	16.24 *W/(m.K)*
Specific heat capacity *(C)*	502.48 *J/(kg.K)*
Thermal expansion (α)	0.0000166 *1/K*
Modulus of elasticity (E)	2×10^{11} *Pa*
Poisson's ration (v)	0.3 (dimensionless)

2) Description of the Grids Used for the Numerical Simulation

For this study, two sets of meshes were created for both the fluid and the structure domains; a coarse and a fine mesh. Description of these fluid and structure meshes are provided in Table 10 and Table 11, respectively. The coarse fluid and structure mesh used are shown next to each other in Fig. 17. Since the location of the shock was known from the experimental data, we have refined the fluid mesh close to the location of the shock to allow for the fluid solver to capture the shock more accurately. The grid spacing in the normal direction at the wall of the cylinder was determined in order to achieve a Y^+ value less than one in the coarse mesh.

The fluid meshes are finer on the interface than the structure meshes, as is usually the case for these types of problems. However, the FSI module used in this work is able to handle this non-matching interface.

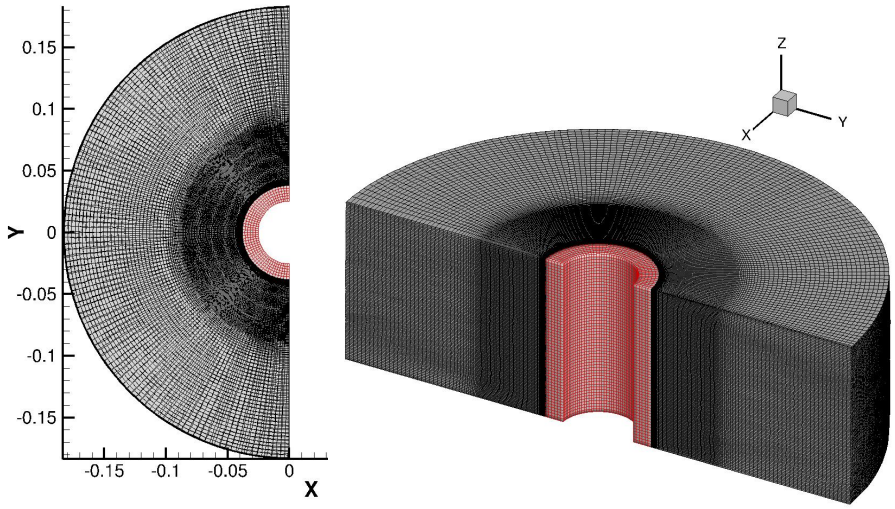

Fig. 17 Fluid and structure coarse meshes for the aero-thermo-elastic analysis problem of hypersonic flow over a leading cylindrical edge (fluid mesh in black and structure mesh in red).

Table 10 Details of the two fluid meshes used in the aero-thermo-elastic analysis for flow over a cylinder.

Fluid Mesh	*Number of nodes*	*Number of elements*	*Type of elements*	*Wall spacing*
Fluid coarse mesh	2,462,400	4,814,740	Prism	10^{-6}
Fluid fine mesh	19,763,866	39,084,360	Prism	6×10^{-7}

Table 11 Details of the two structure meshes used in the aero-thermo-elastic analysis for flow over a cylinder.

Structure Mesh	*Number of nodes*	*Number of elements*	*Type of elements*
Structure coarse mesh	20,706	17,100	Hexahedral
Structure fine mesh	133,055	120,384	Hexahedral

3) Summary of the Applied Numerical Boundary Conditions

The boundary conditions applied to the coupled problem are summarized in Fig. 18. The inner surface of the cylindrical shell is prescribed an isothermal boundary condition since the experimental time is very short. On the outer surfaces of the cylinder (fluid/structure interface), a heat flux is applied on the structure side, and temperature

boundary condition supplied from the structural solver is applied on the fluid side. Since we are simulating only half of the cylinder, an insulated thermal boundary condition is applied at boundary 5 in Fig.18.

For the elastic boundary conditions, we assume that the cylinder is supported rigidly by stands at the leeward side near the tip (boundary 5 in Fig.18). Consequently, the structure can have displacements in the y- and z-directions but not in the x-direction.

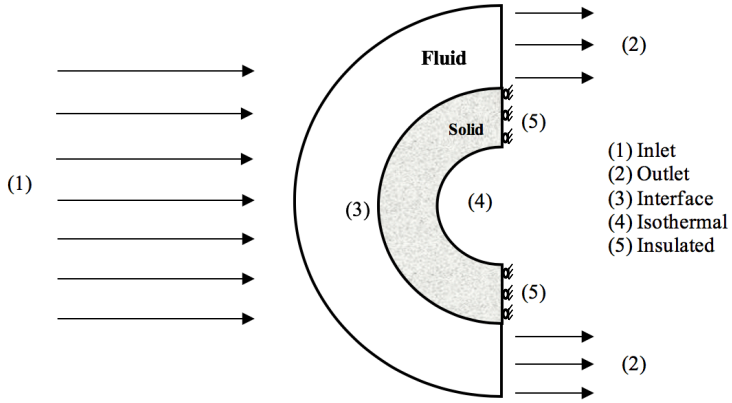

Fig. 18 Applied boundary conditions for the aero-thermo-elastic problem of hypersonic flow over a leading cylindrical edge.

4) Validation of the CFD Solver for High Speed Flows

Here, the main goal is to show that the flow solver is able to capture the physics in the flow-field correctly for high speed flows. The flow solution for pressure obtained from the fine mesh is shown in Fig. 19. The flow-field is characterized by the bow shock that stands off the cylindrical leading edge. The predicted location of the shockwave is at x = - 0.0545*m,* the predicted temperature and pressure behind the shockwave are approximately 2300*K*, and 35000*Pa* respectively, which all compare well with the previous work [9, 10, 52, 53].

The pressure and temperature distributions along the centerline of the upstream flow domains for the fine mesh are shown in Fig. 20 and Fig. 21. The freestream temperature increases suddenly from 241.5*K* to about 2300*K* across the shock and then drops sharply again to the wall temperature 294.4*K* due to the isothermal boundary condition used. This steep temperature gradient happening in a very thin thermal boundary layer, produces a high stagnation point heating rate.

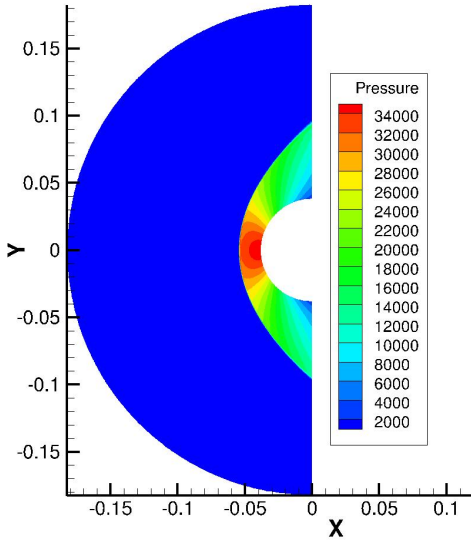

Fig. 19 Pressure contours in the flow field of a cylinder subjected to Mach 6.47 from the uncoupled simulations for the fine mesh.

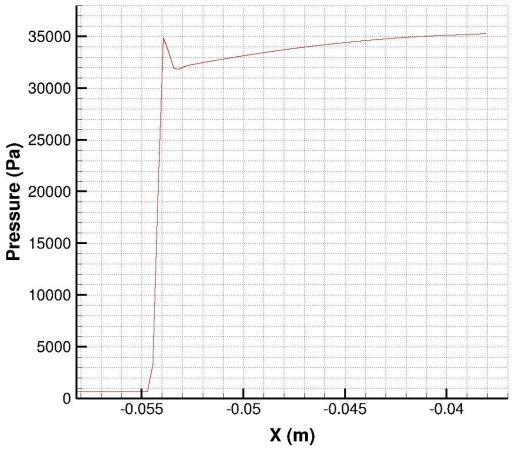

Fig. 20 Fluid pressure distribution along the centerline of a cylinder subjected to Mach 6.47 from the uncoupled simulations for the fine mesh.

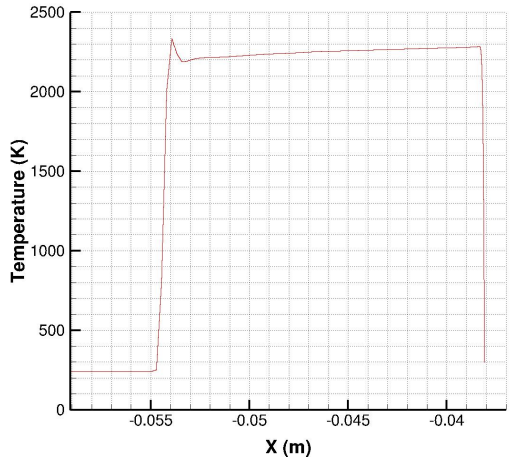

Fig. 21 Fluid Temperature distribution along the centerline of a cylinder subjected to Mach 6.47 from the uncoupled simulations for the fine mesh.

Figure 22 shows the comparison between the computed aerodynamic loads for the uncoupled case along the cylinder surface and the experimental data. This figure shows a good agreement between the computed aerodynamic pressure distribution from both the fine and coarse meshes with the experimental data. The predicted and experimental pressures are normalized by their respective stagnation-point values P_0, which are shown in Table 12. In this table we also have the theoretical (perfect gas) value for the stagnation pressure computed using the normal shock relations. The computed stagnation point pressure solution is very close to the theoretical value calculated as the computational results assume a perfect gas. The results are almost identical for the coarse and fine mesh. The difference between the predicted and experimental stagnation-point pressure is within 7%. This holds for both the fine and coarse mesh.

Table 12 Comparison of the computed stagnation point parameters with experimental data for the cylinder subjected to Mach 6.47 for the uncoupled simulations.

Stagnation point parameters	***Computational-CFD only***		***Experimental***	***Theoretical (perfect gas)***
	Coarse mesh	***Fine mesh***		
Pressure (P_0)	34,995.83 *Pa*	3,5147.66 *Pa*	37921.2 *Pa*	3,5231.16 *Pa*
Heating rate (q_0)	471.68 KW/m^2	469.66 KW/m^2	670 KW/m^2	

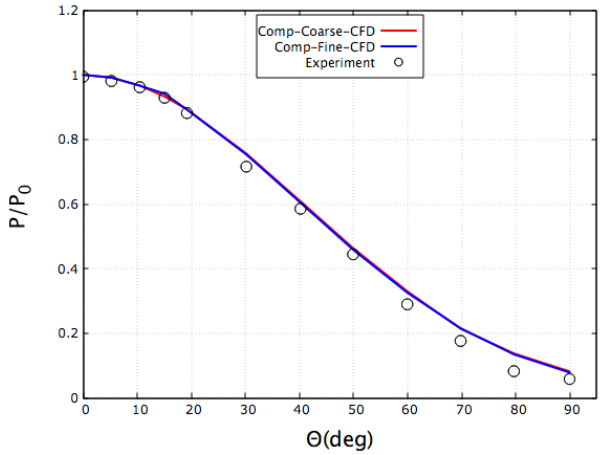

Fig. 22 Comparison of simulated surface pressure distributions with experimental data for the cylinder subjected to Mach 6.47 from the uncoupled simulations for the course and fine meshes.

The main challenge in the fluid analysis is the prediction of the aerodynamic heating rates. This is due to the large temperature gradients which occur in the very thin thermal boundary layer near the cylinder wall. The predicted heating rate distribution for the uncoupled case normalized by the stagnation point heating rate compare well with the experimental results as shown in Fig. 23. The predicted heating rate for the coarse and fine meshes are normalized by their respective stagnation point values q_0, as shown in Table 12. The stagnation point heating rate changes by less than 0.4% between the coarse and fine grids and compares well with the previously computed results from references [9] and [52]. However, as with the results from previous studies, the predicted heating rate is lower than the experimental values as shown in Table 12, which is also the case for the Fay-Riddell and viscous shock layer solutions shown in Table 13.

From these results it can be observed that our solutions are in good agreement with previous CFD work. The difference between the predicted and the experimental heating rate has not yet been resolved by us or others in the past.

Table 13 Stagnation point heating rate from previous work for the cylinder subjected to Mach 6.47 for the uncoupled simulations.

	Fay-Riddell solution [52, 54]	***Viscous shock-layer solution [52, 55]***	***Computational results from reference [9]***	***Computational results from reference [52]***	***Current work-fine mesh***
Stagnation point heating rate (q_0)	482.6 KW/m^2	470.1 KW/m^2	482.6 KW/m^2	485.5 KW/m^2	469.66 KW/m^2

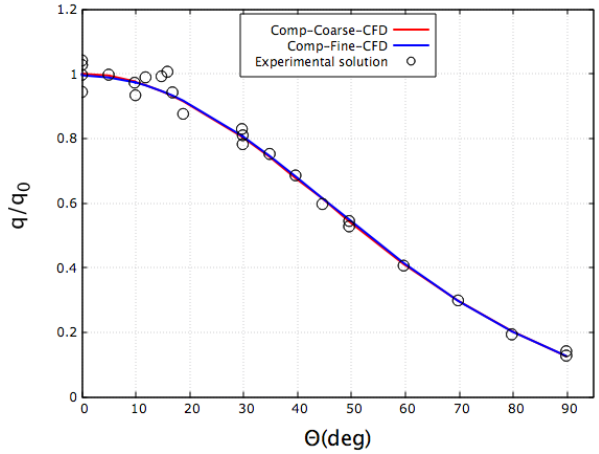

Fig. 23 Comparison of simulated surface heating rate distributions with experimental data for the cylinder subjected to Mach 6.47 from the uncoupled simulations for the course and fine meshes.

5) Validation of the Coupled Analysis Capability

Now we present solutions for the coupled aerodynamic and aero-thermal loads on the cylinder. Following previous work, we assume that the flow field reaches equilibrium instantaneously compared to the thermal response of the cylinder. Hence, the coupled problem is solved in a lagged transient manner; where the flow problem is considered a steady state problem at every time interval. The time step for the thermal solver is taken as 0.1s. Thus, it takes 20 coupling cycles between the fluid and structure solvers to reach the transient solution at t = 2*s*. At each coupling time step a static fluid problem is solved followed by a transient structural and thermal problem.

By taking the aero-thermal coupling into account, the aerodynamic heating rate decreases over time as the surface temperature of the cylinder increases. The stagnation point heating rate decreases in both the coarse and the fine mesh, from t = 0s to t = 2s. These values are presented in Table 14. The drop in the stagnation point heating rate is clear in Fig. 24. The predicted heating rate for the coarse and fine meshes are normalized by their respective stagnation point values q_0, which is the initial heating rate presented in Table 14.

Table 14 Comparison of the computed stagnation point parameters for the cylinder subjected to Mach 6.47 from the coupled analysis at t = 0s and t =2s.

Stagnation point parameters	***Computational-coupled at t = 0s***		***Computational-coupled at t = 2s***	
	Coarse mesh	***Fine mesh***	***Coarse mesh***	***Fine mesh***
Pressure (P_0)	34,995.83 *Pa*	35,147.66 *Pa*	34,997.69 *Pa*	35,147.81 *Pa*
Heating rate (q_0)	471.68 KW/m^2	469.66 KW/m^2	444.07 KW/m^2	438.52 KW/m^2

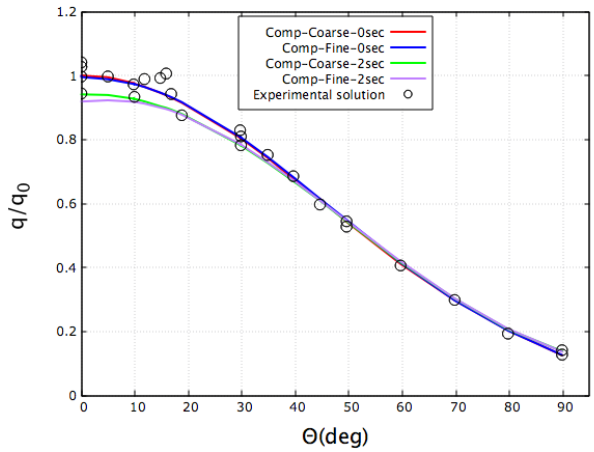

Fig. 24 Comparison of the simulated surface heating rate distributions with experimental data for the cylinder subjected to Mach 6.47 from the coupled analysis at t = 0*s* and t = 2*s*.

Figure 25 shows the evolution of the temperature at the fluid/structure interface for t = 0, 2, 4, 6*s*. It can be seen that the cylinder surface temperature gradually increases with time. This rise in surface temperature creates an overall decrease in the heating rate. Figure 26 shows the evolution of the heating rate distribution as the cylinder temperature rises at t = 0, 2, 4, 6*s*. It can be concluded that the coupled aero-thermal analysis is necessary, otherwise the heating-rate would be overestimated and impacting the requirement on the structure design.

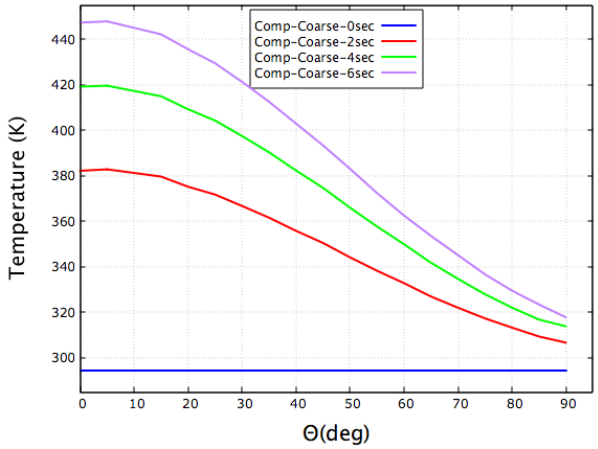

Fig. 25 Time evolution of the surface temperature distributions for t = 0, 2, 4, 6*s* for the cylinder subjected to Mach 6.47 from the coupled analysis for the coarse mesh.

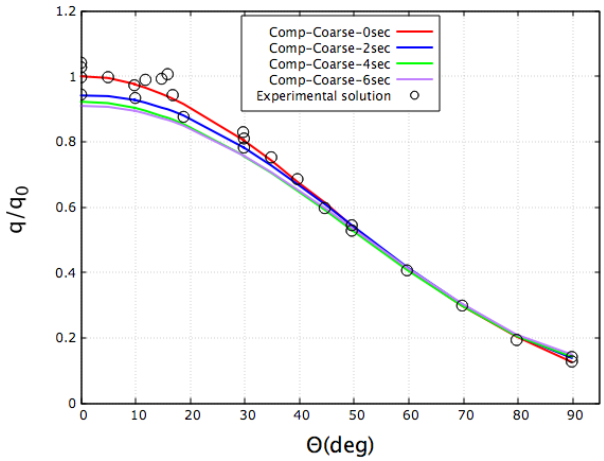

Fig. 26 Time evolution of the surface heating rate distributions for t = 0, 2, 4, 6*s* for the cylinder subjected to Mach 6.47 from the coupled analysis for the coarse mesh.

The cylinder temperature contours from the fine mesh at t = 2*s* are shown in Fig. 27. This figure shows a maximum temperature of about 385*K* at the stagnation point, which matches well with the result from reference [9] at 2*s*. The circumferential thermal stress distribution on the cylinder as computed by AStrO are shown in Fig. 28. These results agree well with the results presented in reference [9]. The maximum stress occurs on the outer surface of the cylinder near the stagnation point and has a value of -198*MPa*. This is due to the high temperature gradients taking place in this region. For this case the deformation and stress are mainly the results of the thermal loads and the effect of the aerodynamic loads can be ignored due to the relatively low dynamic pressure in the experimental setup. The deformation of the cylinder within the profile is negligible compared with the cylinder diameter, because of the relatively low temperature change inside the structure. Hence, the coupling in this problem is primarily between the fluid and thermal solver.

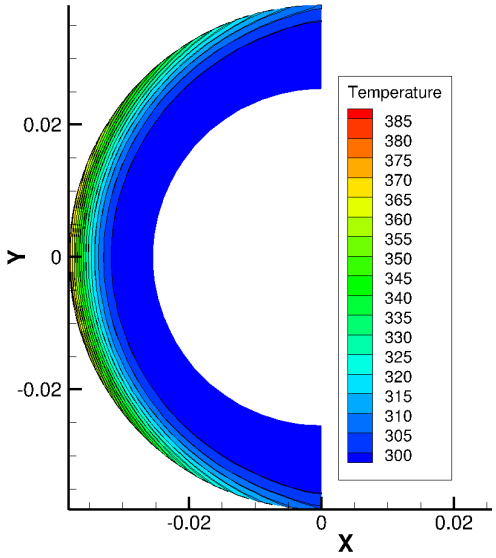

Fig. 27 Temperature contours for the cylinder subjected to Mach 6.47 at t = 2*s* from the coupled analysis for the fine mesh.

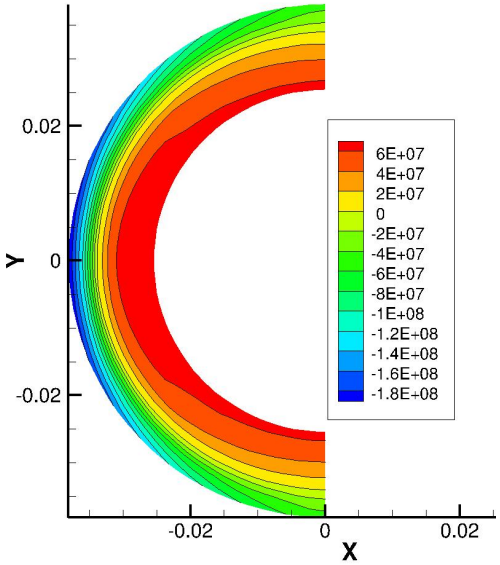

Fig. 28 Circumferential stress contours for the cylinder subjected to Mach 6.47 at t = 2*s* from the coupled analysis for the fine mesh.

B. Aerodynamically Heated Panel

The second application used to validate the aero-thermo-elastic analysis capability is the heated panel case discussed previously. Earlier, we used this example to validate the thermo-elastic capability of AStrO by applying an approximate heat flux on the upper part of the panel. However, in this section we use the aero-thermo-elastic platform to simulate the aerodynamic heating of the panel. Unlike the previous cylinder application, the panel deformations in this case has a significant effect on the flow field. A schematic of the experiment that can be used to validate the flow/thermal/structural analysis as presented in reference [50] is shown in Fig. 29. Two cases for this problem are considered. In the first case, the panel is supported by immovable supports on the bottom corners, and the panel deforms into a concave shape as shown in Fig. 29. In the second case, the panel is supported by immovable supports

at the top corners, and the panel deforms into a concave shape as shown in Fig. 29. The computed results for this case are compared against the numerical solutions from reference [50].

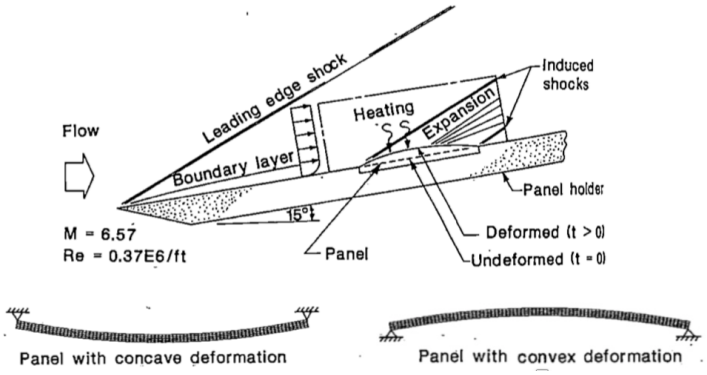

Fig. 29 Schematic diagram of the experiment that can be used to validate the flow/thermal/structural analysis of the aerodynamically heated panel case reproduced from reference [50].

1) Description of the Numerical Set-Up for the Aerodynamically Heated Panel

The coupled aero-thermo-elastic analysis capability is applied to the heated panel case introduced previously. The fluid mesh used for this study has 2,474,940 nodes, with 4,725,000 prism elements. The fluid mesh has a wall spacing of 6×10^{-6}, which gives a Y^{+} of less than one along the panel surface. The structure mesh used in this coupled simulation has 3,216 nodes, with 1,995 hexahedral elements.

The boundary conditions applied to the coupled problem are summarized in Fig. 30. The top surface of the panel, which is the fluid/structure interface, has a surface heat flux applied on the structure side, and an applied temperature enforced from the structure side on to the fluid side. The sides of the panel are considered isothermal, with an applied temperature of 530*R.* The panel case is run with two types of structural boundary conditions. In the first case, the panel is fixed on the left and right edges of the bottom surface, and in the second case the panel is fixed on the left and right edges of the top surface. Numerical results for both cases are presented in the next section.

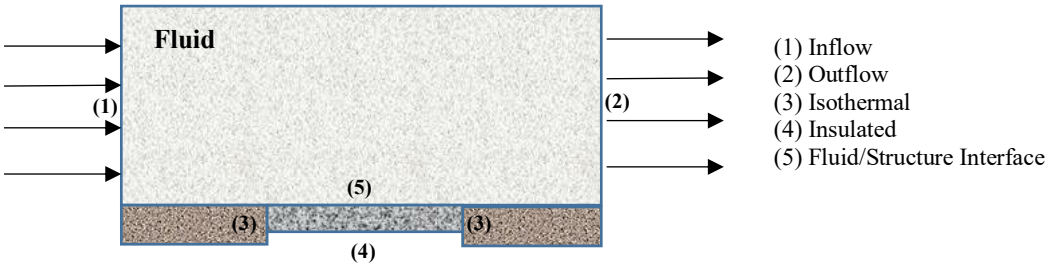

Fig. 30 Applied boundary conditions for the aero-thermo-elastic problem of heated panel.

The panel material and physical properties are given in Table 4 in the thermo-elastic analysis validation section. The initial free-stream flow parameters for this case are described in Table 15. It should be mentioned here that there are two possible flow boundary conditions that can be applied: either we apply the before-shock Mach number 6.47, or the after-shock Mach number of 4.24 with associated post shock conditions. We decided to apply the before-shock Mach number as can be seen in Table 15. Hence, we simulated the flow through the oblique shock in order to obtain the desired boundary layer profile. However, reference [50] does not included any information about the exact length of the front panel holder required to create the precise boundary layer profile. We assumed it to be 5 inches, which later from the results was found to be too small of a value. Due to these reasons the solutions presented in the next section will only be compared qualitatively with reference [50].

Table 15 Initial free-stream conditions for the coupled flow over an aerodynamically heated panel.

Free-stream conditions	***Value***
Free-stream Mach number (Ma_∞)	6.57 (dimensionless)
Wall temperature (T_w)	530 *R*
Free-stream Reynolds number (Re_∞)	0.66×10^6 *1/ft*
Free-stream temperature (T_∞)	530 *K*
Free-stream velocity (U_∞)	6612.3 *ft/s*
Free-stream pressure (P_∞)	0.0971 *psi*

Since the flow field reaches equilibrium much faster than the thermal response of the panel structure, the coupled problem is again solved as a steady-state problem on the fluid side and as a transient problem on the structural side. The time step for the thermal solver is taken as 5s. Thus, it takes six coupled cycles between the fluid and structure solvers to reach the transient solution at thirty seconds.

In the following, computational results for the panel with both convex and concave deformations are presented. Since no experimental data was available for the panel cases, the computed results were validated by comparing against the results in reference [50]. However, as mentioned previously, since certain information about the numerical set-up is lacking, these results are only compared qualitatively.

2) Aerodynamically Heated Panel with Convex Deformation

In this part numerical results from the aero-thermo-elastic analysis of the panel with the convex deformation are presented. The interaction between the panel deformation and the flow density distributions at t = 30*s* for the convex panel is shown in Fig. 31, which plots computed values of density non-dimensionalised by the freestream density. The figure clearly shows the development of a shock originating from the left support on the windward side. The density of the fluid increases through this shock at first but then decreases as the flow expands over the convex panel. A recompression shock is developed as the flow is turned by the deformed panel near the right side. The boundary layer thickness also changes because of the panel deformation. These results agree well qualitatively with the solutions presented in reference [50].

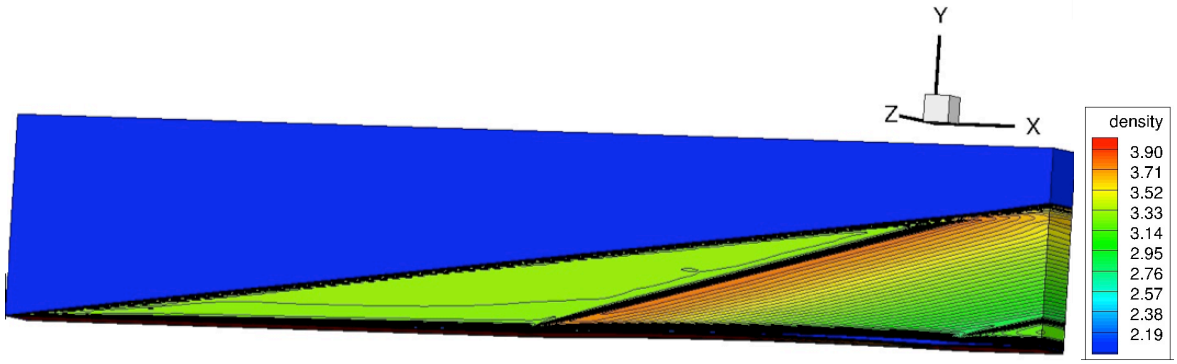

Fig. 31 Flow density distributions at t = 30*s* for the panel with convex deformation.

The evolution of the temperature at the fluid/structure interface at t = 0, 10, 20, 30*s* is presented in Fig. 32 for the panel with the convex deformation. The evolution of the heating rate distribution for the panel with convex deformation is presented in Fig. 33 from t = 0*s*, to t = 30*s*. The overall decrease of the heating rate is due to the rise in the panel temperature shown in Fig. 32. As the temperature of the panel rises, temperature gradient at the fluid/structure interface decreases, which in turn produces a lower heating rate.

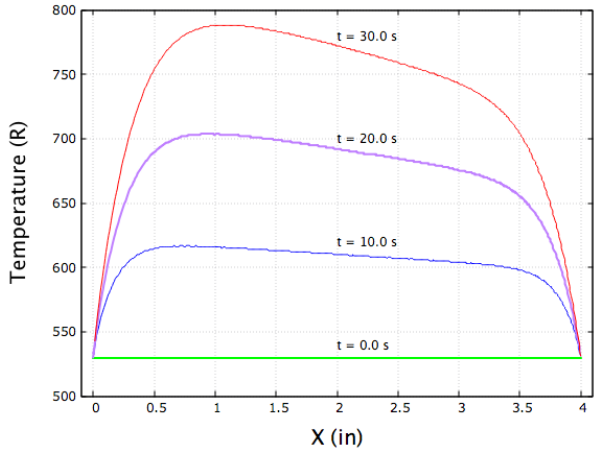

Fig. 32 Evolution of the temperature distribution at the fluid/structure interface for the panel with convex deformation at t = 0, 10, 20, 30*s*.

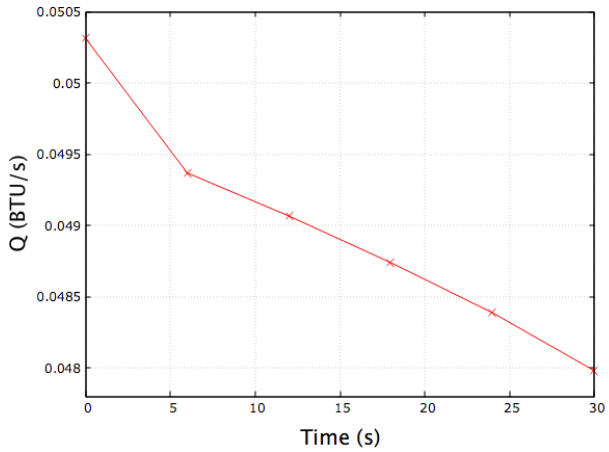

Fig. 33 Evolution of heating rate distribution for panel with convex deformation from t = 0*s* to t = 30*s*.

The results for the temperature and maximum deformations for the convex panel case from the structural solver are shown in Table 16 and Table 17, respectively. The analytical solutions for the temperature and deformation are calculated from Eq.(42) and Eq.(43) presented earlier in the thermo-elastic validation section. The computed results are very close to the analytical solutions. As explained before, the computed results are not exactly the same as the analytical solutions since the analytical equations used are approximate solutions. The computed results from reference [50] also have small variation with respect to the analytical solutions as shown in Table 15 and Table 16.

It can be seen from Table 16 that the computed temperature values are slightly higher than the results from reference [50]. This is due to the shorter length of the upstream panel holder where the boundary layer develops, which was not specified in reference [50]. This in turn results in higher heat transfer rates. The short length of the front panel holder is also the reason for the corresponding higher deflections we have obtained compared to reference [50]. This issue can be addressed in future work.

Table 16 Convex panel temperature solution *T (l/2, t)* in Rankine.

Time(s)	*Coupled computational solution*	*Analytical solution*	*Computational solutions from reference* **[50]**
10	615.58	606.22	595
20	691.47	685.31	650
30	772.859	767.28	705

Table 17 Convex panel deformation *v (l/2, t)* in inches.

Time(s)	*Coupled computational solution*	*Analytical solution*	*Computational solutions from reference* **[50]**
10	0.0126	0.0127	0.0133
20	0.0252	0.0234	0.0239
30	0.0369	0.0336	0.0327

3) Aerodynamically Heated Panel with Concave Deformation

In this section, numerical results from the aero-thermo-elastic analysis of a heated panel case with concave deformation is presented. The flow density distributions at t = 30*s* for the panel with concave deformation is shown in Fig. 34 which compares well qualitatively with the solutions in reference [50]. Figure 34 plots computed values of density non-dimensionalized by the free stream density. For this case an expansion occurs as the flow encounters the left support. This time the flow density decreases through the expansion but starts to increase as the flow is being turned by the concave panel. A second expansion fan emanates from the downwind panel support as the flow is turned back to the horizontal direction.

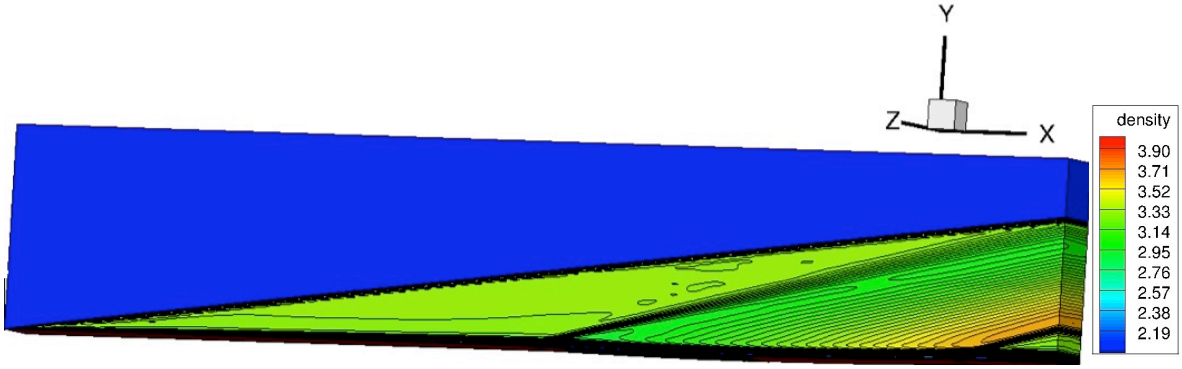

Fig. 34 Flow density distributions at t = 30*s* for the panel with concave deformation.

The evolution of temperature at the fluid/structure interface at t = 0*s* to t = 30*s* is presented in Fig. 35 for the panel with the concave deformation. The evolution of the heating rate distribution from t = 0*s* to t = 30*s* for the concave case is shown in Fig. 36. For the concave case, we again have an overall drop in the heating rate due to the rise of the panel temperature as time passes.

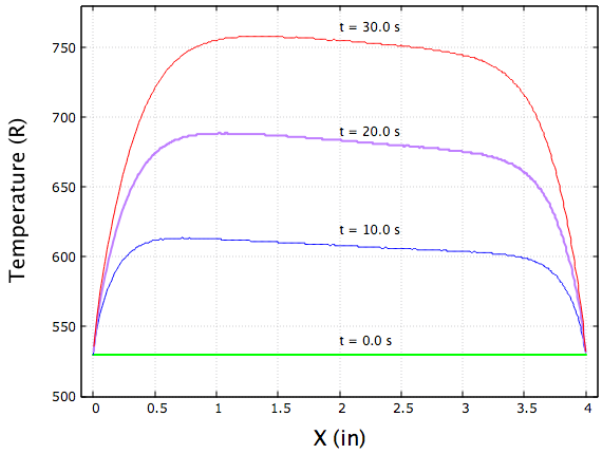

Fig. 35 Evolution of the temperature distribution at the fluid/structure interface for the panel with concave deformation at t = 0, 10, 20, 30*s*.

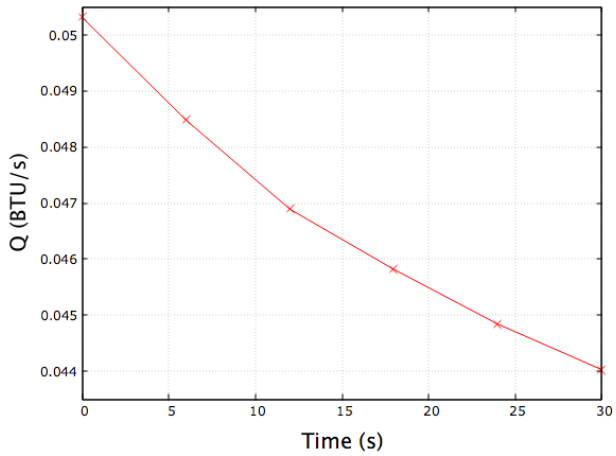

Fig. 36 Evolution of heating rate distribution for panel with concave deformation from t = 0s to t = 30*s*.

The results for the temperature and maximum deformations for the concave panel case from the structural solver are shown in Table 18 and Table 19 respectively. The analytical solutions for the temperature and deformation are calculated from Eq.(42), Eq.(43) presented earlier. Again, the computed results are very close to the analytical solutions but not exactly the same because of the approximations and assumptions made in deriving the analytical solutions. The computed value for the panel deformation at t = 30*s* from reference [50] also has small variation with respect to the analytical solutions as shown in Table 19. The discrepancies in the values of the heating rate and deflection between our results and reference [50] is due to the shorter length of the front panel holder we have used in our simulations and which was not specified reference [50].

Table 18 Concave panel temperature solution *T (l/2, t)* in Rankine.

Time(s)	*Coupled computational solution*	*Analytical solution*
10	608.51	606.22
20	687.22	685.31
30	758.14	767.28

Table 19 Concave panel deformation *v (l/2, t)* in inches.

Time(s)	*Coupled computational solution*	*Analytical solution*	*Computational solutions From reference* **[50]**
10	- 0.0121	- 0.0127	
20	- 0.0238	- 0.0234	
30	- 0.0345	- 0.0336	- 0.031

These two heated panel cases demonstrate the importance of aero-thermo-elastic coupling. Even though very small deformations occurred in the panel, the flow solution is altered significantly. The developed aero-thermo-elastic analysis capability is able to capture the effects of the deformation on the flow quite well.

VI. Conclusion

From the above it can be seen that we have all the components required to run an aero-thermo-elastic analysis problem using the following modules developed in-house and tested previously: the flow solver NSU3D, the thermo-elastic capability from the structural solver AStrO, the FSI module, and the mesh deformation capability. Since the heat transfer solver and the thermo-elastic capabilities of AStrO had not been demonstrated previously, validation results for these modules were presented in this work. The transient aero-thermo-elastic analysis capability was verified through two applications: hypersonic flow over a cylindrical leading edge, and an aerodynamically heated panel. The developed loosely coupled, three-dimensional, aero-thermo-elastic analysis platform which consists of high-fidelity solvers for each discipline will be used for future work in adjoint sensitivity calculations.

Acknowledgments

This work is supported by ONR Grant N00014-17-1-2337. We are grateful for computer time provided by the NCAR-Wyoming Supercomputer Center (NWSC) and by the University of Wyoming Advanced Research Computing Center (ARCC).

References

[1] Slotnich, J., Alonso, J., Darmofal, D., Gropp, W., Lurie, E., and Mavriplis, D. J."CFD Vision 2030 Study: A path to Revolutionary Computational Aerosciences," Center, L. R., NASA, Langley Research Center, Hampton, Virginia, 2014.

[2] Pironkov, P."Numerical Simulation of Thermal Fluid-Structure Interaction," Master of Science thesis, university, Darmstadt, 2010.

[3] Nordstrom, J., and Berg, J. "Conjugate heat transfer for the unsteady compressible Navier-Stokes equations using a multi-block coupling," *Computers & Fluids* Vol. 72, 2013, pp. 20-29. doi: 10.1016/j.compfluid.2012.11.018

[4] Errera, M. P., and Baque, B. "A quasi-dynamic procedure for coupled thermal simulations," *International Journal for Numerical Methods in Fluids* Vol. 72, No. 11, 2013, pp. 1183-1206. doi: 10.1002/fld.3782

[5] Witherden, F., D.;Jameson,A. "Future Directions of Computational Fluid Dynamics," 23rd AIA Computational Fluid Dynamics Conference, Conference, Location, 2017,

[6] Fife, M., E.;Davis,R,L. "A Conjugate Heat Transfer RANS/DES Simulation Procedure," 47th AIAA Aerospace Sciences meeting including the new horizons forume and erospace exposition, Conference, Location, 2009,

[7] Reinert, J. D., Dwivedi, A., and Candler, G. V. "Verification of a conjugate heat transfer tool with US3D," AIAA Scitech 2019, Conference, Location, 2019. doi: 10.2514/6.2019-1892

[8] Seager, C., and Agarwal, R. K. "Hypersonic Blunt-Body Shape Optimization for Reducing Drag and Heat Transfer," *Journal of Thermophysics and Heat Transfer* Vol. 31, No. 1, 2017, pp. 48-55. doi: 10.2514/1.t4650

[9] Dechaumphai, P., Thornton, E. A., and Wieting , A. R."Fluid-Thermal-structural Study of Aerodynamically Heated Leading Edges," NASA Technical Memorandum, NASA, Langley Research Center , Hampton, Virginia, 1988.

[10] Zhao, X., Sun, Z., Tang, L., and Zheng, G. "Coupled Flow-Thermal-Structural Analysis of Hypersonic Aerodynamically Heated Cylindrical Leading Edge," *Engineering Applications of Computational Fluid Mechanics* Vol. 5, No. 2, 2011, pp. 170-179. doi: 10.1080/19942060.2011.11015361

[11] Roe, B., Jaiman, R., Haselbacher, A., and Geubelle, P. H. "Combined interface boundary condition method for coupled thermal simulations," *International Journal for Numerical Methods in Fluids* Vol. 57, No. 3, 2008, pp. 329-354. doi: 10.1002/fld.1637

[12] Miller, B., A."Loosely Coupled Time Integration of Fluid-Thermal-Structural Interactions in Hypersonic Flows," Ph.D Dissertation, Aeronautical and Astronautical Engineering, university, 2015.

[13] Jiao, X. M., and Heath, M. T. "Common-refinement-based data transfer between non-matching meshes in multiphysics simulations," *International Journal for Numerical Methods in Engineering* Vol. 61, No. 14, 2004, pp. 2402-2427. doi: 10.1002/nme.1147

[14] Li, Y. L., Law, Y. Z., Joshi, V., and Jaiman, R. K. "3D common-refinement method for non-matching meshes in partitioned variational fluid-structure analysis," Conference, Location, 2017. doi: 10.1016/j.jcp.2018.05.023

[15] Verstraete, T., Alsalihi, Z., and Van den Braembussche, R. A. "Numerical Study of the Heat Transfer in Micro Gas Turbines," *Journal of Turbomachinery* Vol. 129, No. 4, 2007, p. 835. doi: 10.1115/1.2720874

[16] Verstraete, T., Alsalihi, Z., and Van den Braembussche, R. A. "A comparison of conjugate heat transfer methods applied to an axial helium turbine," *Proceedings of the Institution of Mechanical Engineers, Part A: Journal of Power and Energy* Vol. 221, No. 7, 2007, pp. 981-989. doi: 10.1243/09576509jpe385

[17] Jaiman, R. K., Jiao, X., Geubelle, P. H., and Loth, E. "Assessment of conservative load transfer for fluid-solid interface with non-matching meshes," *International Journal for Numerical Methods in Engineering* Vol. 64, No. 15, 2005, pp. 2014-2038. doi: 10.1002/nme.1434

[18] Cebral, J., and Loehner, R. "Conservative load projection and tracking for fluid-structure problems," 34th Aerospace Science meething and exhibit, Conference, Location, 1996. doi: 10.2514/6.1996-797

[19] Cebral, J., and Lohner, R. "conservative load projection and tracking for fluid-structure problems," *AIAA Journal* Vol. 35, No. 4, 1997, pp. 687-692. doi: 10.2514/2.158

[20] Mavriplis, D. J. "Discrete Adjoint-Based Approach for Optimization Problems on Three-Dimensional Unstructured Meshes," *AIAA Journal* Vol. 45, No. 4, 2007, pp. 741-750. doi: 0.2514/1.22743

[21] Mavriplis, D. J., and Mani, K. "Unstructured Mesh Solution Techniques using the NSU3D Solver," 52nd Aerospace Sciences Meeting, Conference, Location, 2014. doi: 10.2514/6.2014-0081

[22] Mavriplis, D. J., Anderson, E., Fertig, R., and Garnish, M. "Development of a High-Fidelity Time-Dependent Aero-Structural Capability for Analysis and design," 57th AIAA/ASCE/AHS/ASC Structures, Structural Dynamics, and Materials Conference, AIAA SciTech Forum, Conference, Location, 2016. doi: 10.2514/6.2016-1175

[23] Vassberg, J. C., Tinoco, E. N., Mani, M., Zickuhr, T., Levy, D., Broderson, O. P., Eisfeld, B., Wahls, R. A., Morrison, J. H., Mavriplis, D. J., and Murayama, M. "Summary of the Fourth AIAA CFD Drag Prediction Workshop," AIAA, Conference, Location, 2010. doi: 10.2514/6.2010-4547

[24] Vassberg, J. C., Tinoco, E. N., Mani, M., Broderson, O. P., Eisfeld, B., Wahls, R. A., Morrison, J. H., Zickuhr, T., Laflin, K. R., and Mavriplis, D. J. "Abridged Summary of the Third AIAA Computational Fluid Dynamics Drag Prediction Workshop," *Journal of Aircraft* Vol. 45, No. 3, 2008, pp. 781-798. doi: 10.2514/1.30572

[25] Mavriplis, D. J., Yang, Z., and Long, M. "Results Using NSU3D for the First Aeroelastic Prediction Workshop," 51st AIAA Aerospace Sciences Meeting, Conference, Location, 2013. doi: 10.2514/6.2013-786

[26] Mavriplis, D. J., Long, M., Lake, T., and Langlois, M. "NSU3D Results for the Second AIAA High-Lift Prediction Workshop," 52nd AIAA Aerospace Sciences Meeting, Conference, Location, 2014. doi: 10.2514/6.2014-0748

[27] Anderson, E., Bhuiyan, F. H., Mavriplis, D. J., and Fertig, R. "Adjoint-Based High-Fidelity Aeroelastic Optimization of Wind Turbine Blade for Load Stress Minimization," Wind Energy Symposium, AIAA SciTech Forum Conference, Location, 2018. doi: 10.2514/6.2018-1241

[28] Mavriplis, D. J., Fabiano, E., and Anderson, E. "Recent Advances in High-Fidelity Multidisciplinary Adjoint-Based Optimization with the NSU3D Flow Solver Framework," 55th AIAA Aerospace Sciences Meeting, Conference, Location, 2017. doi: 10.2514/6.2017-1669

[29] Mavriplis, D. J. "Solution of the Unsteady Discrete Adjoint for Three-Dimensional Problems on Dynamically Deforming Unstructured meshes," Proceedings of the 46th Aerospace Sciences Meeting and Exhibit, Conference, Location, 2008. doi: 10.2514/6.2008-727

[30] Mani, K., and Mavriplis, D. J. "Geometry Optimization in Three-Dimensional Unsteady Flow Problems using the Discrete Adjoint," 51st AIAA Aerospace Sciences Meeting, Conference, Location, 2013. doi: 10.2514/6.2013-662

[31] Roe, P. L. "Approximate Riemann Solvers Parameter Vectors and Difference Schemes," *Journal of Computational Physics* Vol. 43, No. 2, 1981, pp. 357-372. doi: 10.1016/0021-9991(81)90128-5

[32] Barth, T., and Jespersen, D. "The design and application of upwind schemes on unstructured meshes," 27th Aerospace Sciences Meeting, Conference, Location, 1989. doi: 10.2514/6.1989-366

[33] Anderson, E."Development of an Open-Source Capability for High-Fidelity Thermoelastic Modeling and Adjoint-Based Sensitivity Analysis of Structures," Ph.D Dissertation, Mehcnaical Engineering, university, Laramie, Wyoming, 2019.

[34] "Abaqus," Version 6.14-4 ed., product of Dassault Systems Simulia Corp, Providence,RI,USA, 2017.

[35] Hilber, H. M., Hughes, T. J. R., and Taylor, R. L. "Improved Numerical Dissipation for Time Integratoin Algorithms in Structural Dynamics," *Earthquake Engng Struct. Dynamics* Vol. 5, 1977, pp. 283-292. doi: 10.1002/eqe.4290050306

[36] Samareh, J., A. "Discrete Data Transfer Technique for Fluid-Structure Interaction," 18th AIAA Computational Fluid Dynamics Conference, Conference, Location, 2007. doi: 10.2514/6.2007-4309

[37] Giles, M. B. "Stability analysis of numerical interface conditions in fluid-structure thermal analysis," *International Journal for Numerical Methods in Fluids* Vol. 25, No. 4, 1997, pp. 421-436. doi: 10.1002/(Sici)1097-0363(19970830)25:4<421::Aid-Fld557>3.0.Co;2-J

[38] Joshi, O., and Leyland, P. "Stability Analysis of a Partitioned Fluid–Structure Thermal Coupling Algorithm," *Journal of Thermophysics and Heat Transfer* Vol. 28, No. 1, 2014, pp. 59-67. doi: 10.2514/1.t4032

[39] Roget, B., and Sitaraman, J. "Wall distance search algorithm using voxelized marching spheres," *Journal of Computational Physics* Vol. 241, 2013, pp. 76-94. doi: 10.1016/j.jcp.2013.01.035

[40] Donea, J., Huerta, A., and Ponthot, J. *Encyclopedia of Computational Mechanics*, 2004.

[41] Thomas, P., D., and Lombard, C., K. "Geometric Consevation Law and its Application to Flow Computations on Moving Grids," *AIAA Journal* Vol. 17, No. 10, 1970, pp. 1030-1037. doi: 10.2514/3.61273

[42] Yang, Z., and Mavriplis, D. J. "A Mesh Deformation Strategy Optimized by the Adjoint Method on Unstructured Meshes," 45th AIAA Aerospace Sciences Meeting and Exhibit, Conference, Location, 2007. doi: 10.2514/6.2007-557

[43] Yang, Z., and Mavriplis, D. J. "Higher-Order Time Integration Schemes for Aeroelastic Applications on Unstructured Meshes," *AIAA Journal* Vol. 45, No. 1, 2007, pp. 138-150. doi: 10.2514/1.22847

[44] Bird, R. B., Stewart, W. E., and Lightfoot, E. N. *Transport Phenomena*, Wiley, 2014.

[45] Beck, V. J., Blackwell, B. F., and Clair, C. R. S. *Inverse Heat Conduction Problems*, Wiley-interscience, New York, NY, 1985.

[46] Arpaci, V. S. *Conduction Heat Transfer*, Addison-Wesley, Reading, MA, 1966.

[47] Bejan, A. *Heat Transfer*, John Wiley and Sons, 1993.

[48] Thornton, E., and Dechaumphai, P. "Coupled flow, thermal and structural analysis of aerodynamically heated panels," 1987. doi: 10.2514/6.1987-700

[49] Thornton, E., and Dechaumphai, P. "Finite element prediction of aerothermal-structural interaction of aerodynamically heated panels," 1987. doi: 10.2514/6.1987-1610

[50] Thornton, E., A., and Dechaumphai , P. "Coupled Flow, Thermal, and Structural Analysis of Aerodynamically Heated Panels," *Journal of aircraft* Vol. 25, No. 11, 1988. doi: 10.2514/3.45702

[51] Wieting., A. R."Experimental Study of Shock Wave Interference Heating on a Cylindrical Leading Edge," Ph.D. Disseration, Mechanical Engineering, university, Norfolk, Virgina, 1987.

[52] Zhang, S., Chen, F., and Liu, H. "Time-Adaptive, Loosely Coupled Strategy for Conjugate Heat Transfer Problems in Hypersonic Flows," *Journal of Thermophysics and Heat Transfer* Vol. 28, No. 4, 2014, pp. 635-646. doi: 10.2514/1.t4278

[53] Dechaumphai , P., Thornton, E., A, and Wieting, A., R. "Flow-Thermal-Structural Study of Aerodynamically Heated Leading Edges," *Journal of Spacecraft and Rockets* Vol. 26, No. 4, 1989, pp. 201-209. doi: 10.2514/3.26055

[54] Fay, J. A., and Riddell, F. R. "Theory of Stagnation Point Heat Transfer in Dissociated Air," *Journal of the Aeronautical science* Vol. 25, No. 2, 1958. doi: 10.2514/8.7517

[55] Holcomb, J. E., Curtis, J. T., and Shope, F. L."A New Version of the CVEQ Hemisphere Viscous Shock Layer Problem for Equilibrium Air," Center, A. E. D., Arnold Air Force Station, 1985.